ACS Sustainable Chemistry & Engineering

Research Article

pubs.acs.org/journal/ascecg

Microwave Synthesis of $SnWO_4$ Nanoassemblies on DNA Scaffold: A Novel Material for High Performance Supercapacitor and as Catalyst for Butanol Oxidation

Sivasankara Rao Ede and Subrata Kundu*

Electrochemical Materials Science (ECMS) Division, CSIR-Central Electrochemical Research Institute (CECRI), Karaikudi 630006, Tamil Nadu, India

Supporting Information

ABSTRACT: Self-assembled, aggregated $SnWO_4$ nanoassemblies are formed by the reaction of Sn(II) salt and $Na_2WO_4 \cdot 2H_2O$ in the presence of DNA under microwave heating within 6 min. We have emphasized the natural properties of DNA with its ability to scaffold $SnWO_4$ nanoassemblies and examined the role of starting reagents on the particles' morphology. The diameter of the individual particles is ultrasmall and varies from ~1−2.5 nm. The potentiality of the $SnWO_4$ nanoassemblies has been tested for the first time in two different applications, such as an anode material in electrochemical supercapacitor studies and as a catalyst for the oxidation of butanol to butanoic acid. From the supercapacitor study, it was observed that $SnWO_4$ nanoassemblies with different sizes showed different specific capacitance (C_s) values and the highest C_s value was observed for $SnWO_4$ nanoassemblies having small size of the individual particles. The highest C_s value of 242 F g^{-1} was observed at a scan rate of 5 mV s^{-1} for small size $SnWO_4$ nanoassemblies. The capacitor shows an excellent long cycle life along with 85% retention of C_s value even after 4000 consecutive times of cycling at a current density of 10 mA cm^{-2}. From the catalysis studies, it was observed that $SnWO_4$ nanoassemblies acted as a potential catalyst for the oxidation of butanol to butanoic acid using eco-friendly hydrogen peroxide as an oxidant with 100% product selectivity. Other than in catalysis and supercapacitors, in the future, the material can further be used in sensors, visible light photocatalysis and energy related applications.

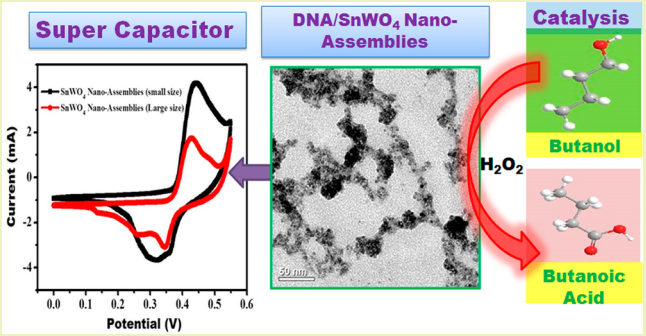

KEYWORDS: *DNA, Nanoassemblies, $SnWO_4$, Catalyst, Supercapacitor*

INTRODUCTION

Research on nanomaterials, mainly nanoparticles (NPs), has been focused on the assembly strategies to control the specific arrangement of NPs. The morphology controlled synthesis of zero and one-dimensional (1-D) inorganic nanomaterials have attracted significant interest due to the importance of the geometrical forms of materials in determining their widely varying properties at nanoscale.[1−3] During the past few years, many techniques have been developed for the successful generation of self-assembled NPs into ordered nanostructures. However, there are very few techniques available to organize nanomaterials in a precise 1-D pattern. The "bottom-up" approach and the wet-chemical synthesis have been found to be the most easy and facile ways to synthesize self-assembled nanomaterials in 1-D patterns in a short time scale. Considering metal oxide nanomaterials in general, they have been extensively studied owing to their unique magnetic, catalytic and energy storage properties across a broad range of fundamental and technological potential. In particular, in fields like energy storage and catalysis, electrochemical supercapacitors show the desirable characteristics of high power density, fast charging, excellent cyclic stability, small size and low mass, when compared with batteries and fuel cells, making them one of the most promising candidates for next generation power devices.[4−7] In general, most commercially available supercapacitors contain high surface area carbonaceous materials. However, they fail to provide sufficient power density or efficiency due to decrease of specific capacitance at higher current densities. To overcome this pitfall, there is a great need to find cost-effective alternate materials with excellent electrochemical properties. Metal oxides show excellent pseudocapacitive properties and among them, binary metal oxides have been reported to exhibit higher performances than single component oxides due to their accomplishable oxidation states and high electronic conductivity. Moreover, they offer many advantages such as low cost, abundant resources and are eco-friendly in nature. Recently, mixed metal oxides, such as $NiWO_4$, $NiCo_2O_4$ and $MnMoO_4$/

Received: July 3, 2015
Revised: August 6, 2015
Published: August 11, 2015

DOI: 10.1021/acssuschemeng.5b00627
ACS Sustainable Chem. Eng. 2015, 3, 2321−2336

$CoMoO_4$, have demonstrated vastly improved performance over single component oxides.[8−10] Beyond these supercapacitors, metal oxides will show great importance in catalysis. In the past few decades, alternative experimental methods with reduced environmental impacts have been developed for many reactions. However, similar progress has not been made on the modification of organic oxidations. Oxidation of alcohol is generally performed with stoichiometric amounts of inorganic oxidants, notably chromium(VI) reagents.[11] These oxidants are relatively expensive and they produce environmentally undesirable byproducts like heavy metal waste. Further, the reactions are often conducted in environmentally undesirable solvents, like chlorinated hydrocarbons. In a constant search for greener technology, there is a definite need for catalytic oxidants where hydrogen peroxide can be used as one of the stoichiometric oxidants,[12] which is atom efficient[13] and produces water as the only byproduct. Most reports involve the oxidation of activated benzylic and allylic alcohols[14] or the use of the Mukaiyama co-oxidation method. Moreover, the reports using non-noble nanomaterials for the oxidation of nonactivated alcohols are scarce; only a few examples have been reported such as the use of palladium,[15] copper,[16] or ruthenium compounds[17] in toluene. To overcome the above limitations, metal oxide nanomaterials are an excellent choice for cost-effective and eco-friendly catalysts for organic oxidation reactions.

Among the various mixed metal oxides, the metals-tungstates are significant due to their special physical, chemical, structural and photoluminescence properties.[18,19] Metal tungstates having the formula MWO_4 mainly crystallizes in two forms, scheelite and wolframite. In scheelite form, tungstate anions have tetrahedral geometry and the ionic radius of the metal is >0.99 Å whereas in wolframite form where the tungstate anions have 6-fold octahedral coordination and the radius is <0.77 Å.[20] Among the various MWO_4, little is known about the crystal chemistry of divalent tin in ternary oxides of metals. This might be due to the low stability associated with the preparation of Sn^{2+}, which tends to oxidize. Hence, these are to be carried out in a closed system. Jeitschko and Sleight first reported $SnWO_4$ to have two polymorphs, an α-phase at low temperature having orthorhombic structure and stable below 670 °C whereas the β-phase exists at high temperatures higher than 670 °C having a cubic structure.[21] The α- and β-phase can be intertransformed by a diffusion-controlled phase-transition mechanism at 670 °C. The decomposition of α-$SnWO_4$ thick films started at a temperature above 550 °C,[22] whereas β-$SnWO_4$ decomposes in air at a temperature above 450 °C.[23]

In the template controlled self-assembly method, the sacrificial molecular guides typically consist of soft materials that can physically guide the nanoscale structures into complex architectures. Among the various molecular guides, the deoxyribonucleic acid (DNA) is possibly the most remarkable molecular guide and potentially used as a structure directing material for creating defined nanomaterials. DNA has special structural features and molecular recognition properties that make it an ideal template to dictate the precise positions of the materials into any deliberately designed structures such as cubes,[24] squares,[25] T-junctions[26] etc. In DNA, there are mainly two binding sites, one is a negatively charged phosphate group and other is the aromatic base molecules. In general, the DNA template construction of self-assembled nanostructures is proceeding via a couple of steps. Initially, the metal cation is attached with the phosphate group in the DNA chain either chemically or electrostatically. Next, the NPs start to grow and assemble along the DNA backbone, resulting in the "organized molecule". Finally, the tethered DNA can form various superstructures due to its well-known base-pairing and supramolecular interactions.

There are different routes that have been exploited for the generation of $SnWO_4$ nanomaterials. The synthesis of $SnWO_4$ was first reported in 1972.[21] Solis and Lantto studied the gas sensing properties of different α-$SnWO_4$ based thick films.[22,23] The same group again reported the phase-structure of α- and β-$SnWO_4$ using different spectroscopic techniques.[27] Dong et al. synthesized α-$SnWO_4$ via a hydrothermal route.[28] Cho et al. studied the photophysical, photoelectrochemical and photocatalytic properties of $SnWO_4$ nanomaterials.[29] Ungelenk and Feldmann synthesized β-$SnWO_4$ nanomaterials via a wet-chemical route.[30] Recently, Su et al. and Huang et al. studied the formation of Zn doped $SnWO_4$ and reduced graphene oxide (RGO)-$SnWO_4$ nanocomposites, respectively and studied their photocatalytic activity.[31,32] Very recently, Pyper et al. synthesized α-$SnWO_4$ thin films electrodes via a hydrothermal route.[33] Most of the above routes reported either require expensive and sophisticated equipment for the synthesis, high temperature, needed expensive chemicals or the resultant product generated a mixture of different shaped NPs with ununiform particles size distribution. Compared to these conventional heating routes, the microwave dielectric heating is advantageous as it reduces the reaction time and energy significantly due to its high penetration and concentrated power. The microwave heating process can heat a substance uniformly by generating homogeneous nucleation sites, which in turn results in the NPs with a better size distribution. Kundu et al. reported earlier the synthesis of metal and metal oxide nanomaterials using microwave heating routes within relatively lower reaction times.[34−38] To the best of our knowledge and from a careful literature search, there is no report for the formation of self-assembled, aggregated $SnWO_4$ nanoassemblies on DNA scaffold within a couple of minutes of microwave heating. Apart from the new way of synthesis, the $SnWO_4$ nanomaterials have shown pronounced electrochemical supercapacitor activity and as a potential catalyst for the butanol oxidation.

In the present report, for the first time we demonstrate the synthesis of self-assembled, aggregated $SnWO_4$ nanoassemblies on a DNA scaffold within 6 min of microwave heating. The $SnWO_4$ nanoassemblies are synthesized by the anion exchange reaction of Sn(II) chloride with sodium tungstate ($Na_2WO_4 \cdot 2H_2O$) in the presence of DNA under microwave heating. The size of the individual $SnWO_4$ NPs on DNA and the chain diameter can be easily controlled by changing the starting reagents concentration and altering various other reaction parameters. The synthesized, self-assembled, aggregated $SnWO_4$ nanomaterials have been used in two potential applications for the first time, one as an anode material in the electrochemical supercapacitor study and the other as a catalyst for butanol oxidation. From the supercapacitor study, it was observed that $SnWO_4$ nanomaterial had different sizes and showed different specific capacitance (C_s) values. The C_s values were found high in the case of $SnWO_4$ particles small in size. The observed C_s value is 242 F/g for small size particles and 217 F/g for large size particles. The cyclic stability study indicates that the C_s value remains stable up to ∼85% even after 4000 consecutive cycles. From the butanol oxidation reaction, it was observed that both $SnWO_4$ morphologies acted as a

DOI: 10.1021/acssuschemeng.5b00627
ACS Sustainable Chem. Eng. 2015, 3, 2321−2336

potential catalyst for the conversion of butanol to butanoic acid at 60 °C temperature with good product yield. The present synthesis process is simple, cost-effective and does not need any toxic chemicals or any sophisticated instruments. In the future, the present route can be extended for the generation of other nanostructured materials within a short time.

EXPERIMENTAL SECTION

Reagents and Instruments. All the chemicals used in this present work were analytical reagent (AR) grade. The tin(II) chloride ($SnCl_2$) and sodium tungstate ($Na_2WO_4{\cdot}2H_2O$) were obtained from Sigma-Aldrich and used as received. Ethanol was purchased from SRL, India. Deoxyribonucleic acid (double-stranded) from herring testes with an average molecular weight ~50 K bp (base pair) was purchased from Sigma-Aldrich. Butanol (99%, Alfa Aser), H_2O_2 (30%, S D Fine Chemicals limited), acetonitrile (CH_3CN, Rankem) were used as received. Polyvinylidene fluoride (PVDF), carbon black, *N*-methyl-2-pyrrolidinone (NMP), nickel foam and potassium hydroxide were procured from Alfa Aesar and used without any further purification. Deionized (DI) water was used for the entire synthesis and application purposes. The synthesized $SnWO_4$ nanoassemblies were characterized using several spectroscopic techniques such as UV−vis absorption spectra, TEM, FE-SEM, XRD, XPS, EDS, FT-IR, TGA-DTA, LASER Raman, ^{1}H NMR analyses, CHI 6304C electrochemical workstation and the detailed specification of all those instruments are elaborated in the Supporting Information section.

Microwave Synthesis of Self-Assembled, Aggregated $SnWO_4$ Nanoassemblies on DNA Scaffold. The $SnWO_4$ nanoassembles are synthesized by the reaction of $SnCl_2$ with $Na_2WO_4{\cdot}2H_2O$ in the presence of DNA under microwave heating for 6 min. In a typical synthesis, a 0.1 M $SnCl_2$ solution was prepared in 100 mL of ethanol. Then in a separate container, 5 mL of DNA solution was mixed with 100 mL of 0.1 M $Na_2WO_4{\cdot}2H_2O$ solution and diluted further by adding 20 mL of DI water. The solution was mixed well by stirring for 20 to 30 min. Then the resultant mixture was put inside a microwave oven and heated for 10 s, taken out and then 4 mL of $SnCl_2$ solution was added at a time while stirring. Again, the solution mixtures were put inside a microwave oven and heated for 10 s and taken out, and again 4 mL of $SnCl_2$ solution was added. This was repeated for a total of 25 times. This was followed by further microwave heating for another 100 s and the total heating time was 350 s (~6 min). The solution was initially light yellowish and during the reaction as well, but after complete reaction, it became dark yellow. The resultant solution was taken out from the microwave oven and cooled at room temperature. The yellowish color precipitate was separated out, washed with ethanol and water for couple of times and centrifuged 2−3 times. The resultant yellowish mass was dried initially at 80 °C. Then the yellowish mass was annealed at various temperatures up to 800 °C for 2 h in a box furnace. Scheme 1 is the schematic representation for the different steps involved in the synthesis of $SnWO_4$ nanomaterials. The resultant solid yellowish powder was used for various analytical characterizations and for the application purposes.

$SnWO_4$ Electrode Fabrication for Electrochemical Supercapacitor Study and Sample Preparation for Catalytic Oxidation of Butanol. The electrochemical studies including cyclic voltammetry (CV), galvonostatic charge−discharge and electrochemical impedance spectroscopy (EIS) were done at room temperature in 3 M KOH solution using an electrochemical workstation CHI 6034C. The EIS measured at an ac voltage of 5 mV amplitude in the frequency range 0.1 Hz to 100 kHz at open circuit potential. The electrochemical cell had three electrode configurations that consist of platinum foil as the counter electrode, Ag/AgCl as the reference electrode and a working electrode. The working electrode was prepared by mixing an electroactive material, carbon black, polyvinylidonedifluride (PVDF), with a ratio of 80:10:10. A small amount of *N*-methyl-2-pyrrolidine (NMP) was added to prepare the slurry and pressed on nickel foam and dried in a vacuum for 12 h at 100 °C; the loading of mass of electroactive material is 2−3 mg. The CV tests were done in the potential window 0−0.55 V at different scan rates varying from 5 to 125 mV s^{-1}. The GCD measurements were measured at different current densities from 1 to 10 mA cm^{-2}. The specific capacitances calculated from CV and GCD curves according to the following equations.[39]

Scheme 1. Schematic Presentation of the Overall Preparation Process for the Formation of $SnWO_4$ Nanoassemblies on DNA Scaffold

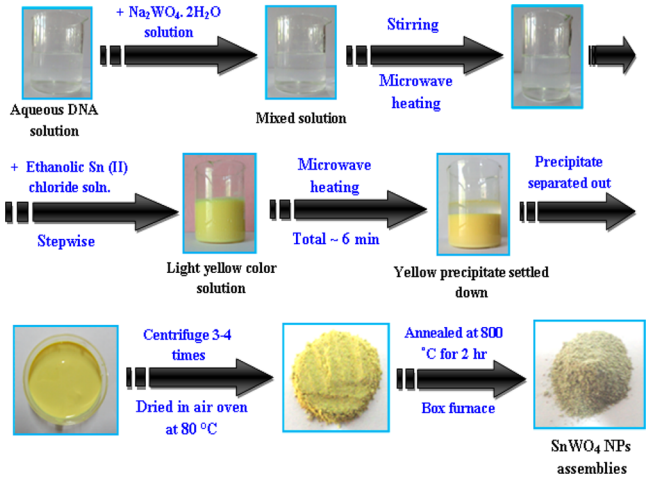

$$C = \frac{\int I(V)\mathrm{d}V}{vm\Delta V} \quad (1)$$

$$C = \frac{I\Delta t}{m\Delta V} \quad (2)$$

where I (A) is the current density used for charge−discharge, Δt is the time elapsed for the discharge cycle, m (g) is the weight of the active electrode material, ΔV is the potential window and v is the scan rate (V s^{-1}). The $SnWO_4$ aggregated nanoassemblies were tested for the catalytic oxidation of the conversion of butanol to butanoic acid. In a typical catalysis reaction, 0.1 mL of butanol in 10 mL of acetonitrile as the solvent was placed in a 15 mL glass vial and 0.1 g of $SnWO_4$ powder and 2 mL of 30% H_2O_2 solution was added. The whole reaction vessel was covered with aluminum foil to avoid the interference of atmospheric oxygen during the reaction. The solution mixture was heated at 60 °C and after 7 h, the characteristic unpleasant smell of butanoic acid was observed indicating the successful formation of butanoic acid. The product was confirmed using UV−vis, ^{1}H NMR, FT-IR and HPLC studies.

RESULTS AND DISCUSSION

Transmission Electron Microscopy (TEM) and Field Emission Scanning Electron Microscopy (FE-SEM) Analysis. The transmission electron microscopy (TEM) images of the self-assembled, aggregated nanoassemblies are shown in Figure 1. Figure 1a−f shows the low and high magnified images of $SnWO_4$ nanomaterials. Figure 1a−c shows the TEM images of the $SnWO_4$ nanomaterials where the individual particles size is small. Figure 1a is the low magnified image and Figure 1b is the high magnified image. As the particles are very small and not clearly visible in the bright field images, we captureed the dark field image also, as seen in Figure 1c. From the image, we can see that the average size of the individual particles is ~1 ± 0.5 nm, the approximate chain diameter is ~9 ± 2 nm and the nominal length of the chains is ~0.8 ± 0.1 μm. From the images, it is clear that the small $SnWO_4$ particles are self-assembled together, aggregated and grown on the DNA chain to generate the chain-like nanoassemblies. The inset of Figure

DOI: 10.1021/acssuschemeng.5b00627
ACS Sustainable Chem. Eng. 2015, 3, 2321−2336

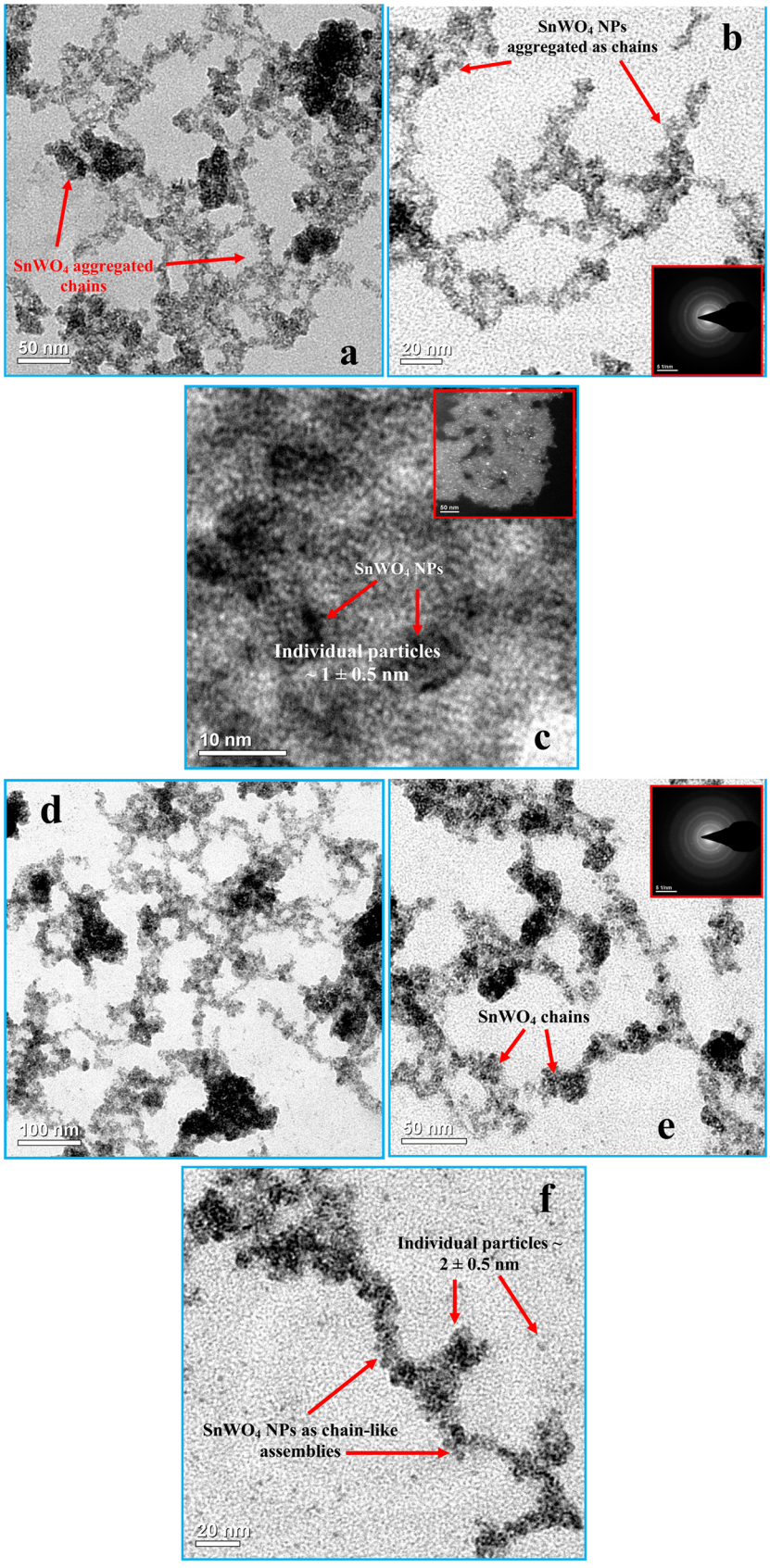

Figure 1. Transmission electron microscopy (TEM) micrographs of the $SnWO_4$ nanoassemblies. Figures 1a–c and d–f are the low- and high magnified TEM images of the $SnWO_4$ nanomaterials where the individual particle size is small and large, respectively. The insets of Figures 1b and e show the corresponding SAED patterns that indicate that the particles are crystalline in nature. The inset of Figure 1c shows the dark field image from the same sample.

DOI: 10.1021/acssuschemeng.5b00627
ACS Sustainable Chem. Eng. 2015, 3, 2321–2336

1b shows the selected area electron diffraction (SAED) pattern, which indicates that the particles are crystalline in nature. Here we did not get any separate intense spots, rather we got high intense ring patterns due to very small size of individual particles. The inset of Figure 1c shows the dark field image from the same sample where the individual particles are visible clearly. Similarly, Figure 1d–f shows the low and high magnified images of the $SnWO_4$ nanomaterials having larger size of the individual particles. Figure 1d shows low magnified images whereas Figure 1e shows high magnified image. Figure 1e shows the image at dark field mode. The size of the individual particles is calculated to be ~2 ± 0.5 nm, whereas the average chain diameter is ~4 ± 1 nm and the nominal length of the chains is ~0.67 ± 0.025 μm. The approximate lengths of the chain are measured from TEM at very low sample concentration (not shown here) using ImageJ software. The inset of Figure 1e shows corresponding SAED pattern, which speaks that particles are crystalline in nature. Here, we can see that small size particles are self-assembled and aggregated to form the chain-like morphology. Figure S-1 (Supporting Information) shows the FE-SEM images of the synthesized $SnWO_4$ nanoassembles of two different sizes. Figure S-1a,b shows the FE-SEM images where the size of individual particles is small and Figure S-1c,d shows the images where the sizes of particles are large. The average diameters of the particles and approximate chain lengths match nicely with TEM analysis as discussed before. From the FE-SEM analysis, it is further clear that small $SnWO_4$ particles are self-assembled aggregated to form the chain-like nanoassemblies.

Optical Absorption Properties and Electronic Band Structure. The optical absorption spectra (UV–vis spectra) of the different solution mixtures for the formation of self-assembled, aggregated $SnWO_4$ nanoassembles are shown in Figure 2A. Curve a in Figure 2A shows the absorption spectrum of only aqueous DNA solution that has a known λ_{max} value at 260 nm due to absorption of aromatic base molecules in its structure. Colorless, aqueous sodium tungstate solution does not show any specific absorption band in the visible region (curve b, Figure 2A). Only ethanolic $SnCl_2$ solution shows a strong absorption band at lower wavelength region at ~205 nm due to ligand to metal transfers (LMCT) spectra (curve c, Figure 2A). The appearance of LMCT band for other metal salts are also observed earlier.[40−43] A mixture of aqueous DNA, sodium tungstate and $SnCl_2$ shows a small hump in the 237 to 331 nm range with a peak maximum at 258 nm (curve d, Figure 2A). The shifting of original DNA peak (curve a, Figure 2A), original tin chloride absorption band (curve c, Figure 2A) and original sodium tungstate absorption band (curve b, Figure 2A) indicates the absorption of Sn^{2+} ions on DNA or their interaction with each other. Similar types of absorption band shifting were absorbed earlier for synthesis of Ag[44] and Os[41] metal NPs. The solid $SnWO_4$ powder was dissolved in DI water, sonicated for 30 min and the aqueous dispersion was measured using UV–vis spectrophotometry. Curves e and f in Figure 2A show the absorption band of $SnWO_4$ nanomaterials having chain-like nanoassemble morphology with large and small size particles, respectively. In both the spectra, we did not see any sharp peak but rather a broad absorption band appeared in the range of 240 to 440 nm. The absorption edge was observed at different values, indicating the change in particle size. A similar type of UV–vis absorption band of $SnWO_4$ was noticed by others in previous reports.[29,32,33] The optical absorption spectrum of $SnWO_4$ in the UV–vis region is

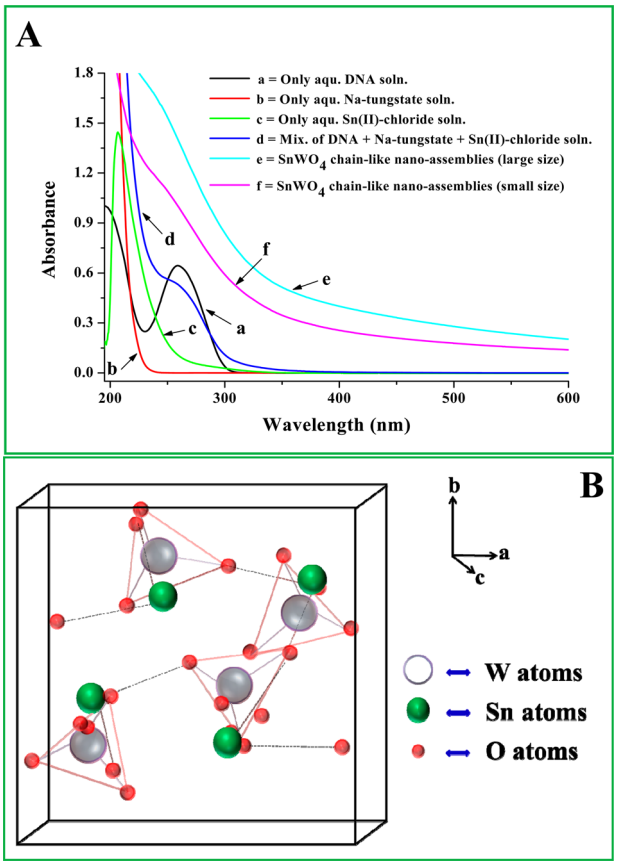

Figure 2. Room temperature (RT) optical absorption spectra (UV–vis spectra) of the different solution mixtures for the formation of self-assembled, aggregated $SnWO_4$ nanoassembles. (A) Curve a shows the absorption spectra of only aqueous DNA solution; curve b is the spectra for aqueous sodium tungstate solution; curve c is the spectra for $SnCl_2$ solution; curve d is the spectra for the mixture of aqueous DNA, sodium tungstate and $SnCl_2$ solution; curve e and f are the absorption band of $SnWO_4$ nanomaterials having chain-like nanoassemble morphology with large and small size of the particles, respectively. (B) Representation of a cubic crystal structure of β-$SnWO_4$ by considering the data of the atomic positions.

due to the excitation of the electron from O 2p to W t_{2g} in the WO_4^{2-} group where the hole on the oxygen and electron on the tungstate atom remain together as an exciton because of their strong interaction. The absorption spectra of the solid $SnWO_4$ samples were also measured by making thin film over the glass substrate, as shown in Figure S-2 (Supporting Information). In Figure S-2, curve a and curve b are the absorption bands for large size and small size $SnWO_4$, respectively. The band gap energy of the two morphologies was evaluated from the Tauc plot where the photoenergy ($h\upsilon$) was plotted with $\alpha h\upsilon$ for the equation, $\alpha h\upsilon = (h\upsilon - E_g)^n$ where α, h, υ and E_g are the absorption coefficient, Planck's constant, photon frequency and photonic energy band gap, respectively. Here n indicates the types of electronic transitions that take place where n is 1/2 for direct allowed and 2 for indirect allowed transition. The observed band gap values for both the morphologies are 1.76 and 2.17 eV for large size and small size $SnWO_4$ nanomaterials, respectively. Cho et al. observed the band gap of β-$SnWO_4$ and was 2.68 eV whereas for α-$SnWO_4$ it was 1.64 eV.[29] Pyper et al. observed an optical band gap of 1.9 eV of α-$SnWO_4$.[33] In our case, the observed band gap is a little higher/lower due to the morphology and the subsequent

DOI: 10.1021/acssuschemeng.5b00627
ACS Sustainable Chem. Eng. 2015, 3, 2321−2336

change in the electronic state in the materials. We also tried to corelate the crystal structure of β-$SnWO_4$ with the electronic band structure. A cubic crystal structure of β-$SnWO_4$ is also depicted by considering the data of the atomic positions reported in the literature,[21,45] as shown in Figure 2B. We see that β-$SnWO_4$ is composed of unshared WO_4 tetrahedra and the SnO_6 octahedra were asymmetric and distorted due to the lone pair effect of Sn(II) ions. As given in the literature, the calculation band gap for α-$SnWO_4$ is 1.65 eV and for WO_3 is 1.77 eV. Considering the crystal structure of $SnWO_4$, the valence band was found hybridized by the Sn 5s and O 2p orbitals due to strong interaction among them.[29] In our case of β-$SnWO_4$, the calculated band gap was 1.76 and 2.17 eV, which is higher than that of the α-$SnWO_4$ and WO_3, probably due to an increase in the crystal field splitting between W and O in WO_4 tetrahedra that led to the shift of the conduction band position at upper region that increases the band gap.

Energy Dispersive X-ray Spectroscopy (EDS) Analysis and X-ray Diffraction (XRD) Analysis. Figure S-3 (Supporting Information) shows the energy dispersive X-ray spectroscopy (EDS) analysis of the as-synthesized $SnWO_4$ chain-like nanoassemblies. The spectrum consists of all the expected peaks originated from the elements Sn, W, O, C, P, N, Na and Cl. The detailed discussions about EDS analysis are presented in the Supporting Information. The X-ray diffraction (XRD) patterns of the synthesized $SnWO_4$ nanoassemblies are shown in Figure 3. The as-synthesized samples are annealed at different temperatures to check the change in crystallinity of the materials. It was observed that $SnWO_4$ particles showed amorphous nature until 600 °C, although at 800 °C they were perfectly crystalline in nature. We already discussed in the Introduction that $SnWO_4$ crystallized to the β-phase above 670 °C. Figure 3A shows the temperature dependent XRD pattern at various annealing temperatures of 80, 300, 400, 500, 600 and 800 °C, respectively. From the pattern, it is observed that up to 600 °C, it shows an amorphous nature. Figure 3B shows the XRD pattern of the $SnWO_4$ nanomaterial annealed at 800 °C. Curve a and curve b show the XRD patterns of the $SnWO_4$ nanoassemblies having large and small size of the individual particles. As the difference between particles size is not much and looks similar for both morphologies. From both the curves, the diffraction peaks originated from the (200), (020), (001) (110), (−112), (022), (−202), (202), (411), (−222), (222), (112), (212), (211), (322), (820) and (811) planes, respectively. The XRD curves are plotted 10−70° for curve A and 15−70° for curve B. All the different diffraction peaks are indexed and match properly with Joint Committee of Powder Diffraction Standards (JCPDS) file number 01-070-1497.[21] At lower 2θ values, we have not observed any other peaks that indicate the absence of any impurities or absence of any other phase in the synthesized nanomaterials. The $SnWO_4$ XRD pattern is indexed as a wolframite cubic structure where tungstate atoms sit inside oxygen tetrahedrons that are not linked together. Solis et al.[27] as well as Ungelenk et al.[30] observed similar types of XRD patterns of β-$SnWO_4$ nanomaterials. So, from the XRD analysis, we confirmed that the synthesized $SnWO_4$ nanomaterials are pure and crystalline in nature.

X-ray Photoelectron Spectroscopy (XPS) Analysis. The X-ray photoelectron spectroscopic analysis was done to identify the chemical and binding state of $SnWO_4$ particles at the surfaces shown in Figure 4. The XPS survey spectrum (Figure 4a) consists of characteristic peaks from Sn (4d) at 26.8 eV, W

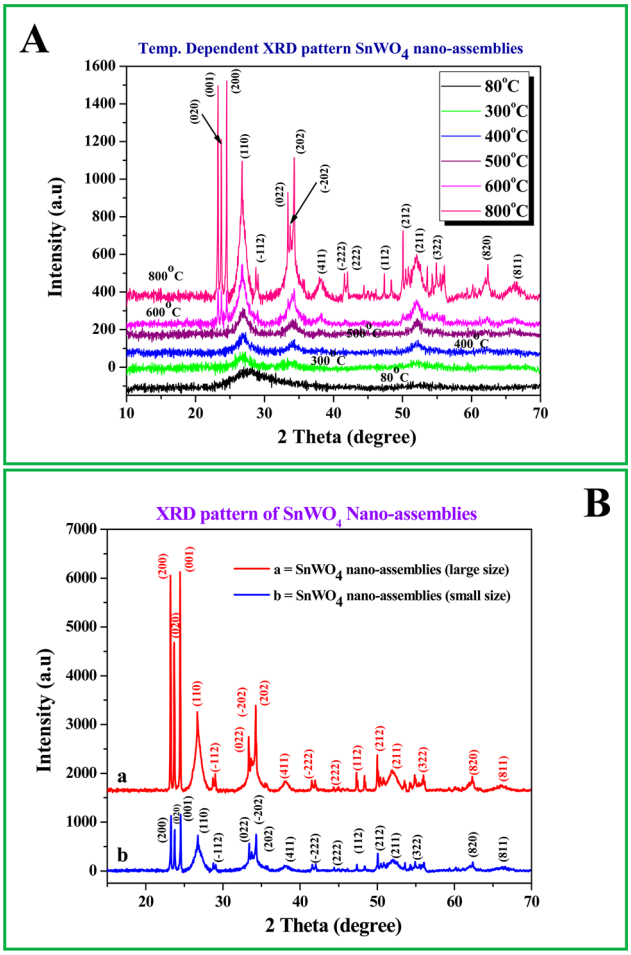

Figure 3. X-ray diffraction (XRD) pattern of the $SnWO_4$ aggregated, chain-like nanoassemblies at various reaction conditions. Figure 3A shows the temperature dependent XRD pattern at various annealing temperatures of 80, 300, 400, 500, 600 and 800 °C, respectively. Figure 3B shows the XRD pattern of the $SnWO_4$ nanomaterial annealed at 800 °C having large (curve a) and small (curve b) individual particles, respectively.

(4f) at 38 eV, P (3p) at 138.5 eV, C (1s) at 285 eV, W (4p) at 428 eV, Sn (3d) at 490.2 eV, O (1s) at 531 eV and Sn (3p) at 713.8 eV, respectively. Figure 4b−f shows the high resolution XPS scan for Sn (3d), W (4f), O (1s), C (1s) and P (3p) peaks, respectively. In the high resolution Sn (3d) XPS peak, Sn $3d_{3/2}$ and Sn $3d_{5/2}$ peaks appeared at binding energies 494.9 and 486.4 eV, respectively (Figure 4b). All the high resolution peaks are fitted with peak sum and background to get a clear idea about the specific peak position and oxidation state of the elements. Figure 4c shows the high resolution spectrum for W (4f) where W $4f_{5/2}$ and W $4f_{7/2}$ peaks appeared at binding energies of 38.8 and 36.7 eV, respectively. Figure 4d shows the O (1s) high resolution XPS spectrum where the peak appeared at a binding energy of 530.4 eV. Figure 4e shows the XPS spectrum for C (1s) where the peak appeared at 284.8 eV. Figure 4f shows the high resolution peak for P (3p) where the P $3p_{1/2}$ and P $3p_{3/2}$ peaks appeared at binding energies of 140.5 and 138.02 eV, respectively. The appearance of the P (3p) peak in XPS spectrum indicates the presence of P with our synthesized $SnWO_4$ nanomaterials that came from DNA used during our synthesis. Similar types of XPS spectral feature was

DOI: 10.1021/acssuschemeng.5b00627
ACS Sustainable Chem. Eng. 2015, 3, 2321−2336

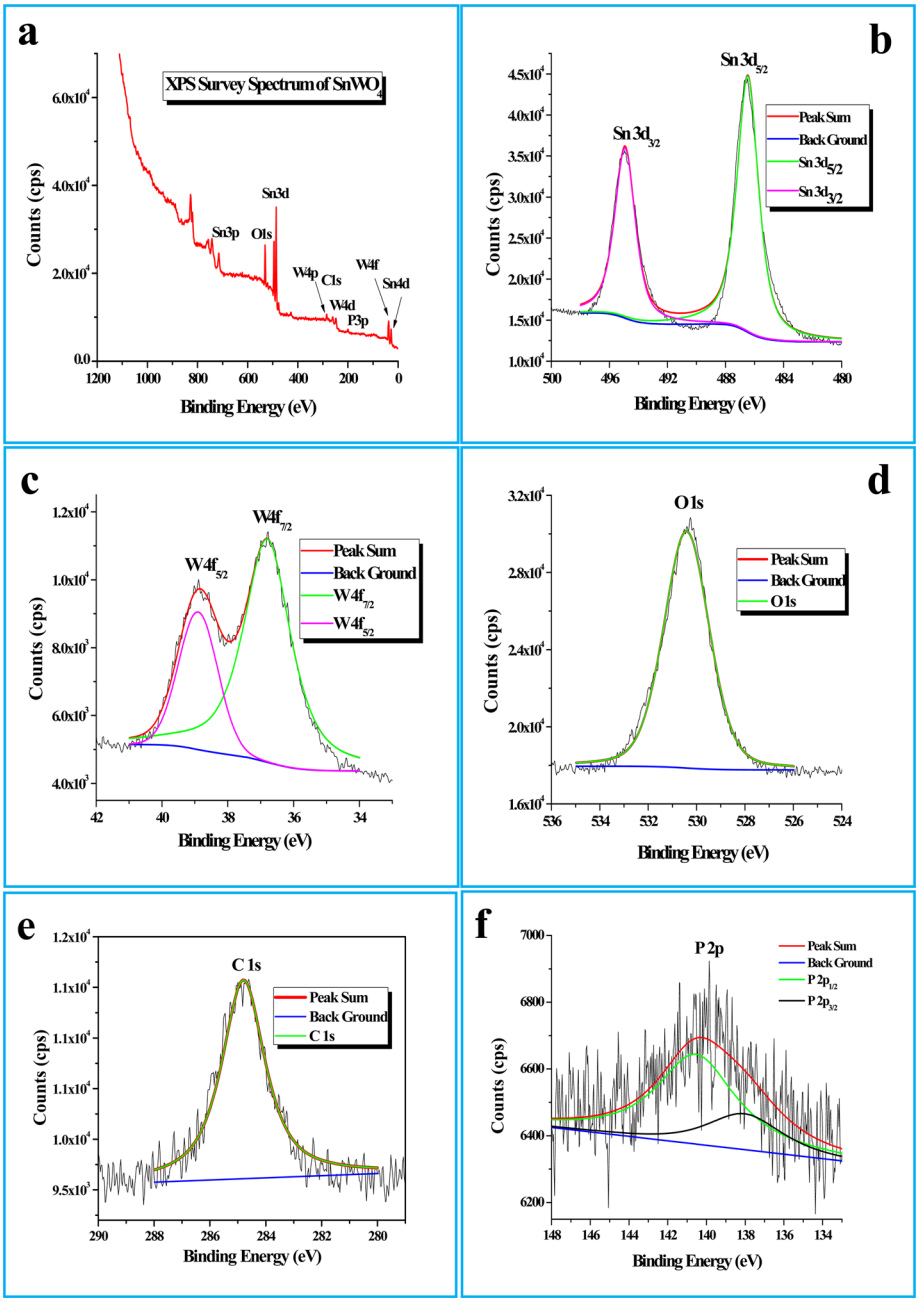

Figure 4. X-ray photoelectron spectroscopy (XPS) analysis of $SnWO_4$ aggregated, chain-like nanoassemblies. Figure 4a shows the survey spectrum; Figures 4b–f show the high resolution XPS scans for Sn (3d), W (4f), O (1s), C (1s) and P (2p) peaks, respectively.

reported earlier by Cho et al., Dong et al. and Huang et al. for their study of $SnWO_4$ nanomaterials.[28,29,32]

Laser Raman Analysis of the $SnWO_4$ Nanoassemblies on DNA Scaffold. The Laser Raman spectra of the self-assembled, aggregated $SnWO_4$ nanoassemblies on DNA scaffold are shown in Figure 5. In Figure 5, curve a indicates the Raman spectrum for $SnWO_4$ having large size whereas curve b indicates the Raman spectrum for $SnWO_4$ having small size. In both cases, the spectra are taken after annealed at 800 °C. In both the curves, 4 intense bands are located almost at the same positions at 974, 807, 714 and 273 cm^{-1}, respectively. All these Raman peaks had confirmed the successful formation of $SnWO_4$ nanomaterials. Solis et al. observed the Raman bands of β-$SnWO_4$ almost similar position and in addition of 4 high intense peaks, few other low intense peaks also observed as they run the sample in a vacuum.[27] Thangavel et al. observed similar Raman bands as we observed and confirmed the composition of β-$SnWO_4$ nanomaterials.[46] It was also reported earlier for MWO_4, the highest intense Raman band observed above 900 cm^{-1} is due to stretching vibration modes caused by each of the six W–O bonds in WO_6 octahadrons. Moreover, it also observed from the group theory analysis is that for the wolframite MWO_4, in particular for $ZnWO_4$, 36 lattice vibrations are possible where 18 even vibrations are Raman active.[47]

Thermal Analysis Study of the $ZnWO_4$ Nanoassemblies on DNA Scaffold. The thermogravimetric analysis (TGA) and differential thermal analysis (DTA) of the as-synthesized $SnWO_4$ nanoassemblies are shown in Figure 6, curve A and curve B, respectively. The TGA-DTA analysis is a

DOI: 10.1021/acssuschemeng.5b00627
ACS Sustainable Chem. Eng. 2015, 3, 2321–2336

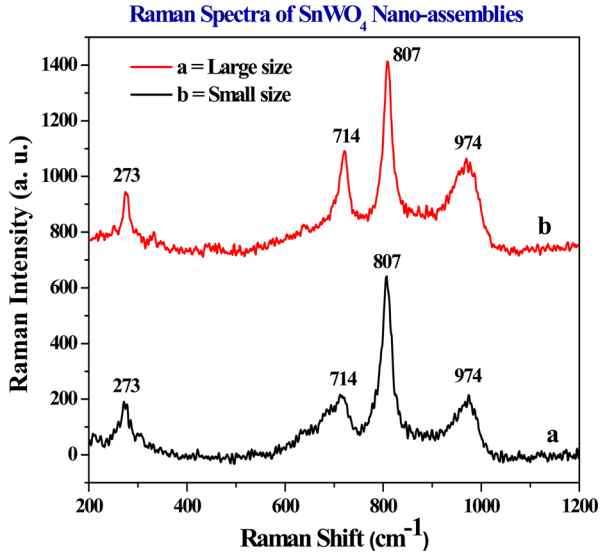

Figure 5. Laser Raman spectra of larger size (curve a) and smaller size (curve b) $SnWO_4$ aggregated nanoassemblies.

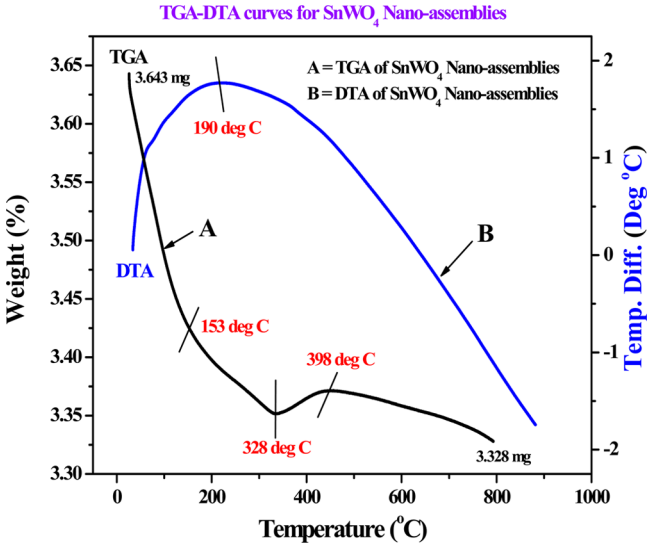

Figure 6. Curve A and curve B are the thermogravimetric analysis (TGA) and differential thermal analysis (DTA) of the $SnWO_4$ nanoassemblies.

sophisticated tool to determine the thermal stability and crystallinity of the synthesized product. From the TGA curve, we can see that there is a steep decrease in weight loss up to 328 °C. The initial weight loss up to 153 °C is probably due to removal of water molecules or may be due to the moisture in the sample. After that, the weight loss up to 328 °C is due to removal of excess chemicals or excess DNA from the samples. After 328 °C, gain in weight is observed up to 350 °C and after 460 °C, and then the gradual weight loss continues up to the end. The increase in weight up to 450 °C is probably due to slow phase transition and the simultaneous absorption of moisture at the same temperature. From curve a, we can see that we have started our experiment with 3.643 g of sample and after heating up to 800 °C, the amount of sample remaining is 3.328 g. So, the % of weight loss is 8.8%. From the DTA curve given as curve B, a broad exotherm is observed between 100 and 300 °C. A peak is observed at 190 °C, probably due to the change in crystallinity or the phase change. Similar types of thermal results were reported earlier by others for their synthesis of MWO_4 nanomaterials.[46,48]

FT-IR Analysis. The Fourier-transform infrared (FT-IR) spectra of only DNA and DNA bound $SnWO_4$ nanomaterials are shown in Figure 7. In Figure 7, curve a is the FT-IR

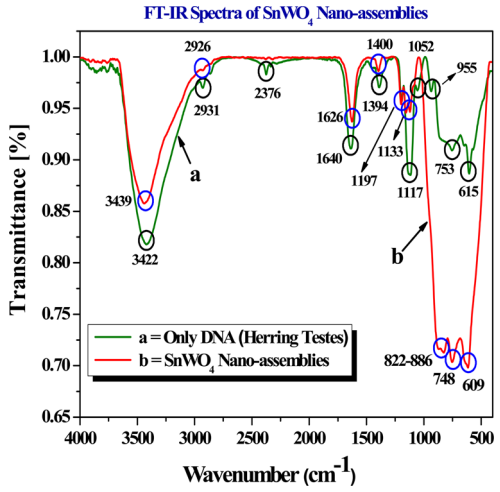

Figure 7. Fourier-transform infrared (FT-IR) spectra of only DNA (curve a) and DNA bound $SnWO_4$ nanoassemblies (curve b).

spectrum of only DNA and curve b is the FT-IR spectrum of DNA bound $SnWO_4$ nanoassemblies. We plotted the spectrum of DNA with the DNA bound $SnWO_4$ to make a comparative study and to study the probable interaction of the nanomaterial with DNA. It was discussed earlier that positively charged metal ions or metal NPs can attach with the negatively charged phosphate group present in DNA. From curve a, we can see a few low intense peaks in lower wavenumber regions at 615, 642, 753 and 955 cm^{-1}, which are attributed to the stretching vibration of the phosphate group in the parent DNA molecule. All these specific bands of DNA are either not observed or shifted from their earlier positions in the case of DNA bound $SnWO_4$ (curve b), which indicates the probable interaction between them. The peaks observed for DNA (curve a) at 1052 and 1117 cm^{-1} are attributed to the structural vibrations of C−O−C or C−C bonds that are shifted to a high wavenumber region in the case of DNA bound $SnWO_4$ nanomaterials. A peak appeared at 1394 cm^{-1} in the case of only DNA (curve a) and shifted to 1400 cm^{-1} in the case of DNA bound $SnWO_4$ nanomaterials. The observed peak at 1394 cm^{-1} is due to an asymmetric stretching vibration of the PO_2^- group. A sharp peak observed at 1640 cm^{-1} for DNA is due to the stretching vibration of the carbonyl group. The same peak shifted to 1624 cm^{-1} in the case of DNA bound $SnWO_4$ nanomaterials. Another sharp peak for DNA is observed at 2931 cm^{-1} due to the symmetric stretching vibration of C−H bonds in the $-CH_2$ group, which shifted to 2926 cm^{-1} in the case of DNA bound $SnWO_4$ nanomaterials. The high intense and broad peak observed at 3422 cm^{-1} in the case of only DNA sample shifted to 3439 cm^{-1} in the case of DNA bound $SnWO_4$, which is due to the stretching vibration of the O−H group in DNA or in water. In the case of curve b for DNA bound $SnWO_4$ sample at the lower wavenumber region 3−4, sharp and high intense peaks are observed that are either shifted or not present in the case of the only DNA sample. The positions of these peaks are 609, 748, 822−886 cm^{-1}, respectively, which are mainly due to the presence of $SnWO_4$ nanomaterials on DNA. The peaks at

DOI: 10.1021/acssuschemeng.5b00627
ACS Sustainable Chem. Eng. 2015, 3, 2321−2336

Table 1. Detailed Final Concentrations of All the Reagents, Reaction Parameters, Time of Reaction and Particle Size and Shape

set no.	final conc. of DNA (M)	final conc. of Sn(II) chloride solution (M)	final conc. of $Na_2WO_4 \cdot 2H_2O$ solution (M)	time of microwave heating (min)	shape of the particles	chain diameter and length	average particles size (nm)
1	1.3×10^{-2}	4.0×10^{-2}	4.0×10^{-2}	6	chain-like, NPs assemblies	$D = 9 \pm 2$ nm, $L = 0.8 \pm 0.10$ μm	~1 ± 0.5
2	2.7×10^{-3}	4.0×10^{-2}	4.0×10^{-2}	6	chain-like, NPs assemblies	$D = 4 \pm 1$ nm, $L = 0.67 \pm 0.025$ μm	~2 ± 0.5

Scheme 2. Formation Mechanism and Binding of Sn(II) Ions to DNA for the Generation of Different Sizes of $SnWO_4$ NPs on DNA Scaffold

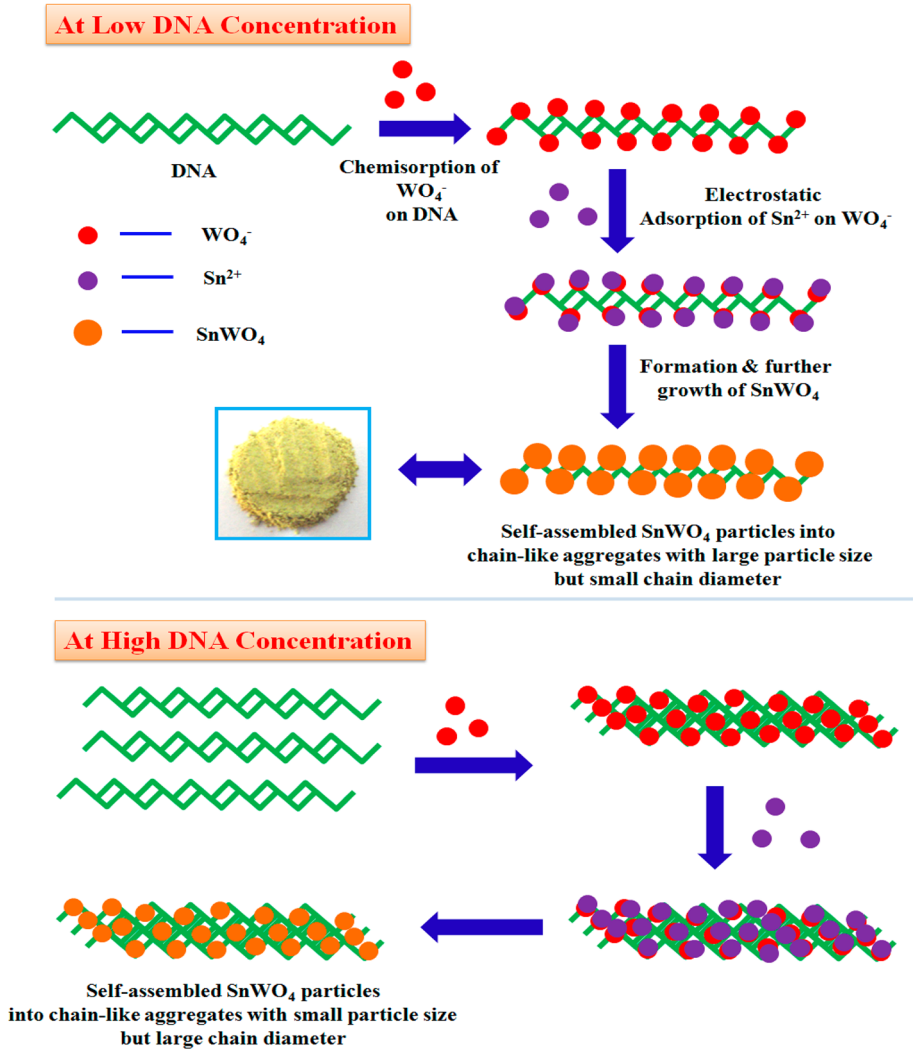

822 and 886 cm^{-1} are attributed to the stretching vibration of W−O−W bridging bonds in $SnWO_4$.[49] The peaks at 609 and 748 cm^{-1} are probably due to the asymmetric stretching vibration of the WO_6^{6-} group and the stretching mode of W−W bonds. It was reported before that there was a peak at ~450 cm^{-1} observed due to the bending vibration of $(WO_6)^{6-}$ octahedron in MWO_4, but this was not observed in our present study. The FT-IR vibration bands observed in our study are nicely matching with the earlier reports.[8,50,51] Table S-1 (Supporting Information) shows the different FT-IR bands, experimentally observed bands for only DNA and the reported FT-IR bands for DNA with the corresponding band assignments.[52] After analysis of the FT-IR spectrum, it was confirmed that $SnWO_4$ nanoassemblies are formed and bound on the DNA molecule.

Reaction Mechanism for the Formation of $SnWO_4$ Nanoassemblies on DNA Using Microwave Heating. Self-assembled, aggregated, chain-like $SnWO_4$ nanoassemblies are synthesized via the reaction of Sn(II) salt with $Na_2WO_4 \cdot 2H_2O$ in the presence of DNA under 6 min of microwave heating. Two different morphologies of $SnWO_4$ having small and large individual particles formed by varying the reagents concentration are shown in detail in Table 1. From Scheme 1, we can observe that $SnWO_4$ particles are successively formed and annealed the sample at 800 °C. In our synthesis, the presence of DNA is extremely important for the formation and growth of self-assembled structure and their stabilization after formation. We did some control experiments as follows, first we did the same reaction without DNA and observed that $SnWO_4$ NPs formed but immediately agglomerated without any specific

DOI: 10.1021/acssuschemeng.5b00627
ACS Sustainable Chem. Eng. 2015, 3, 2321−2336

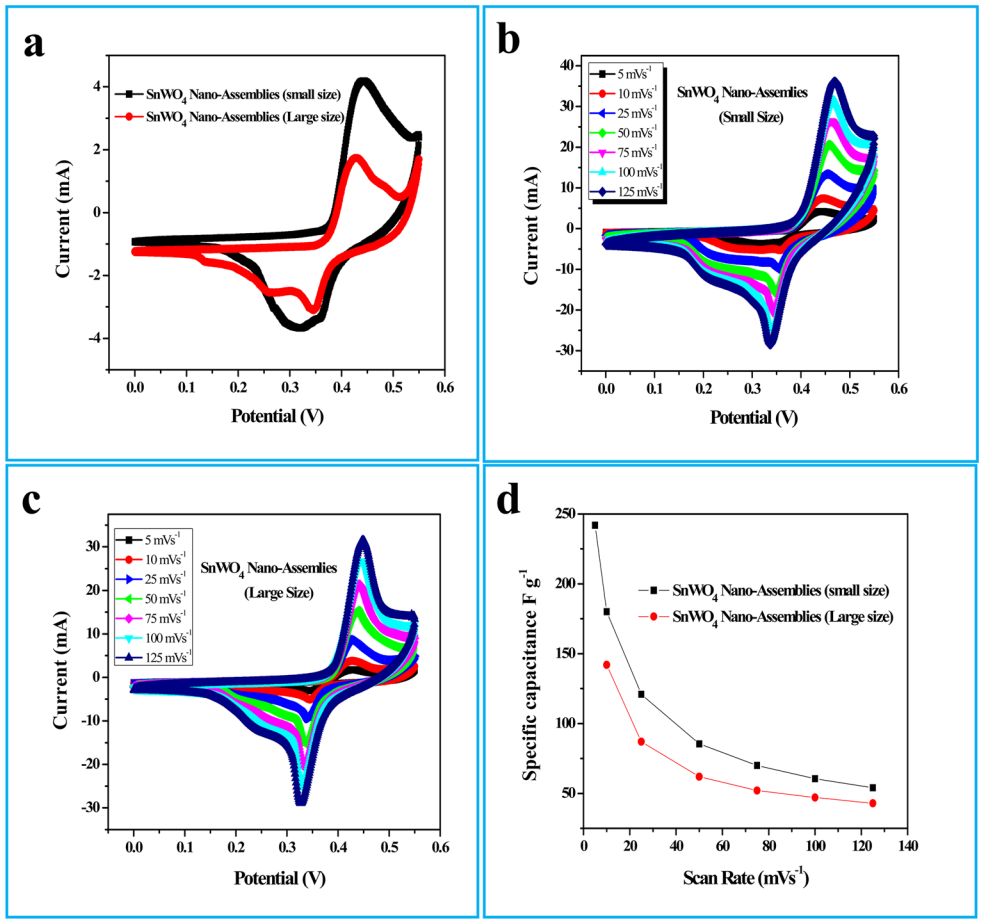

Figure 8. (a) Cyclic voltammogram (CV) curves of small and large size $SnWO_4$ electrodes at 5 mV s^{-1}; Figures 8b and c are the CV curves of small and large size $SnWO_4$ electrode at various scan rates; Figure 8d shows specific capacitance as a function of scan rate for small and large size $SnWO_4$ electrodes.

morphology (TEM images are not shown here) due to the absence of any capping agent. Moreover, microwave heating also plays a crucial role for the quick formation, nucleation and growth of the particles in a chain-like fashion. When the same reaction was done by conventional heating, it took longer time and the resultant particles were not uniform in shape. For our synthesis, we used Sn(II) chloride as a tin precursor. Tin(II) chloride in anhydrous form is not fully soluble in water but soluble in ethanol, methanol, ether and tetrahydrofuran. $SnCl_2$ has a layered structure having a boiling point of 623 °C and melting point of 247 °C and density of 3.95 g/cm^3. In hot water, it readily hydrolyzes and forms a $Sn(OH)_2$ precipitate. In our synthesis, we also measured the pH values of the different solution mixtures and studied their role for the synthesis of $SnWO_4$. The pH of the DNA solution is 3.37, only ethanolic $SnCl_2$ solution is 1.05, only $Na_2WO_4{\cdot}2H_2O$ solution is 9.70, a mixture of DNA, $SnCl_2$ and $Na_2WO_4{\cdot}2H_2O$ is 7.78. The pH values of the $SnWO_4$ NPs solution from which two different morphologies were obtained at the end are 7.04 and 7.23, respectively. The actual chemical reaction that takes place in our synthesis is just the anion exchange reaction between the precursors:

$$Na_2WO_4{\cdot}2H_2O + DNA \rightarrow DNA{-}WO_4^{2-}\ \text{complex}$$

$$DNA{-}WO_4^{2-}\ \text{complex} + SnCl_2 \rightarrow DNA{-}SnWO_4\ (\text{nuclei}) + NaCl + H_2O$$

$$DNA{-}SnWO_4\ (\text{nuclei}) \xrightarrow{\text{growth}} SnWO_4@DNA\ (\text{self-assembled } SnWO_4\ \text{nanoassemblies})$$

The successful formation of $SnWO_4$ nanomaterials on a DNA scaffold is schematically depicted in Scheme 2. From the above reaction and from Scheme 2, we can see that initially WO_4^{2-} ions are chemically adsorbed on the DNA and once Sn(II) salt was added, Sn^{2+} ions electrostatically interact with WO_4^{2-} ions that are already attached with DNA. Then, through the chemical interaction, Sn^{2+} ions react with WO_4^{2-} ions, $SnWO_4$ nuclei are formed and then grown over DNA and generated the $SnWO_4$ NPs as chain-like morphology. From the UV–vis spectra (Figure 1) and from the FT-IR analysis (Figure 7), we observed the sign of adsorption of metal ions with the DNA molecule. From the FT-IR analysis, we confirmed that the negatively charged phosphate group, the deoxyribose sugar unit and the aromatic base molecules participate during the binding action of the materials with the DNA molecule. From Table1 and Scheme 2, we can see that at low DNA concentration, the individual $SnWO_4$ particles are formed comparatively large in diameter whereas the resultant chain diameter is less. On the other hand, at high DNA concentration, the individual size of the $SnWO_4$ particles is

DOI: 10.1021/acssuschemeng.5b00627
ACS Sustainable Chem. Eng. 2015, 3, 2321−2336

less whereas the resultant chain diameter is large. We assume that at a low DNA concentration, the small $SnWO_4$ nuclei get more space to grow and after certain time they did. At higher DNA concentration, the individual $SnWO_4$ nuclei get restricted during their growth and this results in small size $SnWO_4$ particles. Then, the formed $SnWO_4$ crystalline particles grow on the DNA present in the solution gets self-assembled and resulted in the aggregated, chain-like morphology. Ungelenk and Feldmann noticed a different mechanism for their formation of cubical $SnWO_4$ microcrystals in CTAB surfactant media.[30] They observed that β-$SnWO_4$ having a NaCl-like crystal structure grew more along the (100) facet compared to the (110) facets and resulted in the cubical structure. Gao et al. also proposed a mechanism for their formation of $BaWO_4$ nanomaterials on a DNA scaffold.[40] They observed that initially Ba^{2+} ions bound with the phosphate backbone and the oxygen of WO_4^{2-} ions interact preferentially with amino moieties of adenine due to the hydrogen bonding interaction. Then, WO_4^{2-} ions reacted with Ba^{2+} ions to generate the $BaWO_4$ nuclei on DNA bases. Then, the $BaWO_4$ nuclei grew initially to adjacent areas and finally along the length of the DNA and generated the chain-like morphology. In our present study also, we postulate that initially, Sn^{2+} ions react with WO_4^{2-} ions and generate $SnWO_4$ nuclei and then $SnWO_4$ nuclei grow on DNA. The growth of $SnWO_4$ nuclei takes place in multiple steps on DNA present in solution. Initially, small $SnWO_4$ nuclei crystallized in the preferential direction, and then they aggregated and stabilized on the DNA chain. Finally, all the $SnWO_4$ particles are self-assembled on the DNA chain and generated the chain-like $SnWO_4$ nanoassemblies. Hence, in our present synthesis of $SnWO_4$, DNA acted in a dual role: initially it helped during nucleation and the growth process and finally it stabilized the synthesized particles in chain-like morphology. The stabilization of DNA bound metal and metal oxide nanomaterials have been previously highlighted.[8,35,41−44] Then, by taking the self-assembled aggregated $SnWO_4$ nanoassemblies, we carried out two specific applications: one as a potential anode material in electrochemical supercapacitor studies and the other as a catalyst for room temperature oxidation of butanol to butanoic acid as described below.

Electrochemical Measurements of $SnWO_4$ Nanoassemblies. Figure 8a illustrates the CV curves of the $SnWO_4$ nanoassemblies with small and large size at a scan rate of 5 mV s^{-1}, in the voltage window 0 to 0.55 V. A pair of strong redox peaks in the CV curves is observed for both the small and large size $SnWO_4$ nanoassemblies indicating the fast redox reaction in $SnWO_4$ nanoassemblies. The measured capacitance is mainly governed by faradaic redox mechanism, and the reaction is based on the reversible redox of Sn^{2+} to Sn^{4+}.

$$Sn^{2+} \underset{\text{Discharge}}{\overset{\text{Charge}}{\rightleftharpoons}} Sn^{4+} + 2e^-$$

Here the pseudocapacitance behavior comes mainly from the faradic redox reaction of Sn and the role of W is to enhance the electrical conductivity of the $SnWO_4$ materials. The redox behavior of W has no contribution to the measured capacitance. This is in good accordance with the Pourbiax diagram of W and previous reports.[54] When compared small size with large size $SnWO_4$ nanoassemblies, it showed an increase in current intensity that indicated that small size had the highest specific capacitance. From eq 1, we calculated the specific capacitance values of both small and large size $SnWO_4$ nanoassemblies, which were 242 and 217 F g^{-1} at 5 mV s^{-1}, respectively. The small size $SnWO_4$ nanoassemblies exhibited the higher capacitance compared to large size $SnWO_4$, which is mainly due to their higher surface area as confirmed from BET analysis and short diffusion path length providing easy access of ions/electron transport with the active materials to achieve higher specific capacitance. Figure S-4 (Supporting Information) shows the nitrogen adsorption−desorption isotherm profile consists of a typical type IV isotherm with a distinct hysteresis loop observed for small size $SnWO_4$ nanoassemblies. The specific surface area (SSA) for small size $SnWO_4$ nanoassemblies is calculated from the Brunauer−Emmett−Teller (BET) analysis that is 78.25 m^2 g^{-1} with a total pore volume of 0.25 cm^3 g^{-1}. Barrett−Joyner−Halenda (BJH) analysis indicates that the pores have mainly mesoporous structure with a pore size distribution of 2−7 nm. Such a pore size distribution is favorable to improve the electrochemical behavior of the small size $SnWO_4$ nanoassemblies electrode due to the unhindered diffusion and accession of electrolyte ions into the inner space/matrix.[55] The BET SSA for large size $SnWO_4$ nanoassemblies is calculated to be 34.98 m^2 g^{-1}. To evaluate the relationship between the scan rate and specific capacitance performance of small and large size $SnWO_4$ nanoassemblies, the CV studies were performed at different scan rates (5−125 mV s^{-1}). We have seen that the obvious increase of peak current while increasing the scan rate indicates a good rate capability of $SnWO_4$ nanoassmblies.[56] Figure 8b,c shows the CV curves of the small and large size $SnWO_4$ nanoassemblies at various scan rates. From both figures, it was observed that the positions of the anodic and cathodic peaks shifted to higher and lower potentials, which might be due to the ionic diffusion rate as it was not fast enough to keep pace with electronic neutralization in the redox reaction.[57] Figure 8d shows the relation between scan rate with change in specific capacitance. From Figure 8d, we can observe that the specific capacitance value decrease with the increase of the scan rate might be due to that some electroactive surface areas became inaccessible (diffusion limited), leading to less availability of electrode surface area for ion diffusion and adsorption due to inadequate time.[58]

Figure 9a shows the changes in the specific capacitance of the $SnWO_4$ nanoassemblies (small size) at various current densities (1−10 mA cm^{-2}). All of the GCD curves show the symmetric and nonlinear behavior with various current densities, further confirming the pseudocapacitive behavior of the electrodes. From these charge−discharge curves, the specific capacitance was calculated at various current densities using eq 2. It can be seen that the specific capacitance values of both electrodes decrease with the increase of current density. This may be due to some active material in the surface becoming inaccessible for charge storage at higher current densities.[58] For comparison, the GCD curves of both small and large size $SnWO_4$ nanoassemblies at a current density of 1 mA cm^{-2} are shown in Figure 9b. The voltage plateaus in charge/discharge process are well matched with the peaks observed in the CV curves (Figure 8a). Compared to large size, the small size of the $SnWO_4$ electrode showed the higher discharging rate, which demonstrates the higher specific capacitance of the electrode. The calculated specific capacitance values of the large and small size of $SnWO_4$ electrodes are 125 and 75 F g^{-1}, respectively at a current density of 1 mA cm^{-2}. We have checked the rate capability of our electrode at high current densities such as 6, 8, 10 and 15 mA cm^{-2} and observed that the specific capacitance

DOI: 10.1021/acssuschemeng.5b00627
ACS Sustainable Chem. Eng. 2015, 3, 2321−2336

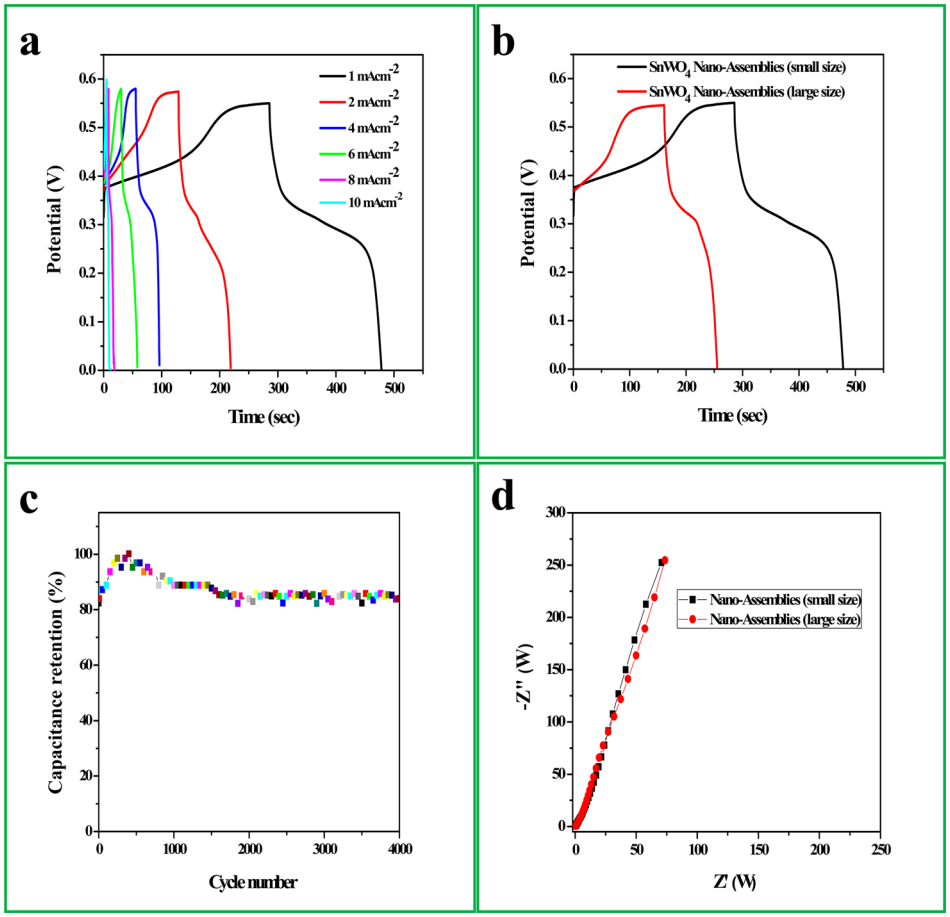

Figure 9. (a) Galvanostatic charge/discharge (GCD) curves of small size $SnWO_4$ electrodes at various current densities; (b) GCD curves of small and large size $SnWO_4$ electrode at 1 mA cm^{-2} current density; (c) cyclic performance of small size $SnWO_4$ electrode at 10 mA cm^{-2} for 4000 cycles; (d) Nyquist plots of the small and large size $SnWO_4$ electrode.

Table 2. Comparison for the Charge−Discharge (CD) Capacitance of the Synthesized Material with Previous Reports

set no.	name of the material	structure	specific capacitance (CD)	current density	reference
1	$MnMoO_4/CoMoO_4$	nanowires	187 F g^{-1}	1 A g^{-1}	10
2	$NiWO_4$/DNA	nanochains	45 F g^{-1}	0.2 mA cm^{-2}	8
3	$ZnWO_4$/DNA	nanochains	39 F g^{-1}	0.2 mA cm^{-2}	39
4	$CoMoO_4$/MWCNT	nanocomposites	170 F g^{-1}	0.1 A g^{-1}	59
5	$SnWO_4$/DNA	nanoassemblies	125 F g^{-1}	1 mA cm^{-2}	current report

values are 64, 49, 43.7 and 27 F g^{-1}, respectively. We have compared our specific capacitance value from charge−discharge curves with previous reports. As there are no reports for the supercapacitor study on $SnWO_4$, we compared our result with other similar materials as summarized in Table 2.[8,10,39,59] As it is well-known, a long cycle life is the most important factor for supercapacitor application, so an endurance test based on $SnWO_4$ nanoassemblies (small size) was conducted by GCD at 10 mA cm^{-2} current density as shown in Figure 9c. Until the first 400 cycles, a small increase in capacitance was observed that might be due to the activation process occurring at the beginning of the charging/discharging test with the electrolyte. With the increasing time, it gradually penetrates into the electrode more and subsequently more electrode material gets activated, contributing to the increase in specific capacitance.[60] After 400 cycles, the capacitance tends to slow down and the electrode material maintained ∼85% of its initial capacitance even after 4000 consecutive times of cycling, implying that our working electrode has a good cyclic stability. So, our synthesized $SnWO_4$ nanoassemblies on DNA scaffold as electrode or device material were found extremely efficient, having good cyclic stability, being straightforward and robust. Apart from these, the electrochemical impedance spectroscopy (EIS) analysis was also done to understand further the conductive performance of as-prepared electrodes. Figure 9d shows the EIS results, and from the results it could be observed that both of the plots are exhibiting the semicircle arc at the high frequency region followed by a straight line in the low frequency region. The semicircle arc at the high frequency region indicating the interfacial charge transfer resistance (R_{ct}), which is about 5.38 Ω for larger size and 4.68 Ω for smaller size $SnWO_4$ electrodes. The straight line in the low frequency region indicates the Warburg resistance, which results from the frequency dependence of ion diffusion/transport in the electrolyte.[61] Figure S-5 (Supporting Information) shows the behavior of EIS of small size $SnWO_4$ nanoassemblies before

DOI: 10.1021/acssuschemeng.5b00627
ACS Sustainable Chem. Eng. 2015, 3, 2321−2336

and after 4000 cycles. There is not much increase in the R_{ct} value (before cycling, 4.68 Ω; after cycling, 7.52 Ω) as observed, which indicates the better electrochemical behavior and higher rate capability of our working electrode.

Catalytic Oxidation of Butanol to Butanoic Acid Using $SnWO_4$ Nanoassemblies as Catalyst. For the past few years, transition metal and metal oxide nanomaterials have been receiving much more attention in the field of catalysis. Recently, our group reported the catalytic activity of Osmium organosol and β-MnO_2 nanomaterials in the hydrogenation of cyclohexene to cyclohexane and conversion of aniline hydrochloride to emaraldine salt in aqueous solution, respectively.[42,62] In our report, for the first time we used $SnWO_4$ nanoassemblies on DNA scaffold as a catalyst and hydrogen peroxide as an oxidant for the oxidation of butanol to butanoic acid using acetonitrile as a solvent at 60 °C in 7 h. The chemical reaction for the catalysis study is

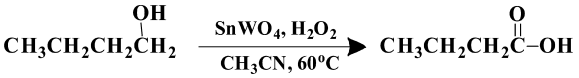

In the catalysis reaction, 0.1 mL of butanol in 10 mL of acetonitrile as the solvent was placed in a 15 mL glass vial and 0.1 g of $SnWO_4$ powder and 2 mL of 30% H_2O_2 solution was added. The reaction vessel was covered with aluminum foil to avoid the interference of atmospheric oxygen during the reaction and heated at 60 °C for 7 h. After 7 h, the characteristic unpleasant smell of butanoic acid was observed indicating the formation of butanoic acid, which was further confirmed using UV–vis, ^{1}H NMR, FT-IR and HPLC studies. In our reaction, initially some of the $SnWO_4$ nanomaterial oxidized by H_2O_2 to form $Sn(WO(O)_2(OH)_2)$.[63] The oxidized form of the $SnWO_4$ nanomaterial plays a key role for the oxidation of butanol to butanoic acid, as shown below.

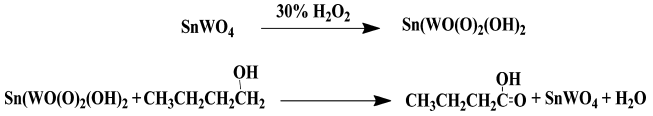

In Figure 10A, curve a shows the FT-IR spectrum of butanol and curve b shows the FT-IR spectrum of butanoic acid. In curve a, the peaks nearly at 3364, 2946, 1457, 1383 and 1061 cm^{-1} appeared signifying the peaks of butanol. In curve b, the peaks nearly at 3450, 2971, 2260, 1724, 1584 and 1054 cm^{-1} appeared whereas the peak at 1724 cm^{-1} is attributed to C═O stretching frequency, the peak at 2971 cm^{-1} is attributed to C—H stretching frequency of the alkane group, the peak at 1054 cm^{-1} is attributed to the stretching frequency of C—O of the acid group. Here, in the case of curve b, the appearance of a new peak at 1724 cm^{-1} was attributed the oxidation of butanol to butanoic acid. Figure 10B, shows the ^{1}H NMR spectrum of butanoic acid and acetonitrile mixture in the $(CD_3)_2SO_4$ solvent. The singlet at δ 1.98 ppm is attributed to the $-CH_3$ group in acetonitrile and the singlet at δ 3.32 is due to interaction of $(CD_3)_2SO_4$ solvent with residual water. The peak at δ 4.52 ppm is due to residual water byproduct from hydrogen peroxide, the peak at δ 2.48 ppm is attributed CH_2-CO, the peak at δ 1.31 ppm is attributed to the $-CH_2$ group and at δ 0.84 ppm due to the $-CH_3$ group. The characteristic peak for acidic proton appears at δ 10.97 ppm, which confirms the oxidation of butanol to butanoic acid.[64] In Figure 10C, curve a shows UV–vis absorption spectrum of butanol and curve b shows the absorption spectrum of butanoic acid. In curve a, an intense peak appeared at ∼191 nm due to alcoholic group. In curve b, the peak appeared at ∼195 nm which is due to the $n-\pi^*$ transition of the carboxyl group. In general, the saturated carboxylic acids show a λ_{max} value near 200 nm and in our case we observed the peak at ∼195 nm. The HPLC study was done with starting material and final product, using methanol as the solvent. The R_f value for starting material is 3.21 and for the final product is 3.26, which matches the reference butanoic acid R_f value. From the chromatogram, we have calculated the yield and selectivity of our product. The observed yield was found to be ∼60% with 100% selectivity. We have conducted a couple of controlled experiments to check the influence of acetonitrile, DNA, $SnWO_4$ in the oxidation reaction. We have carried out the reaction in the absence of $SnWO_4$ but in the presence of hydrogen peroxide and observed no reaction within the experimental time scale. We also checked the reaction without heating just by stirring at room temperature (RT) keeping all other reaction parameters the same but found that butanoic acid was formed but with less yield compared to the reaction done in heating conditions at 60 °C. We carried out the reaction without hydrogen peroxide and observed that the catalytic reaction did not take place at all in our experimental time scale. All these control experiments led us to the conclusion that all reagents are extremely important to carry out the reaction. We tried initially the oxidation of 1,4 butandiol with our synthesized catalyst but we did not get a desired product and rather observed a mixture of aldehyde, acid and ester. This might be due to presence of two alcoholic groups in the same chemical environment. We also checked the solvent effect on the catalytic reaction, using water as solvent in place of acetonitrile; very less yield was obtained due to the partial solubility of butanol in water. We have conducted postreaction studies to check the recyclability of the catalyst by doing the same reaction again and again for 10 consecutive times by heating the catalyst every time up to 200 °C to remove the residues of previous reaction. As the butanoic acid reached boiling point, ∼165 °C, it was found that with up to 6–7 cycles the catalytic behavior was not decreased much. However, after the first cycle of catalysis, the time taken by the catalyst slowly increased cycle to cycle, which might be due to deactivation of the catalyst because of overoxidation of the active sites.[65−68]

CONCLUSION

In conclusion, we have studied the properties of DNA and its ability to scaffold $SnWO_4$ nanoassemblies and examined the influence of starting reagents concentrations on the particles' morphology. We observed that self-assembled, aggregated $SnWO_4$ nanoassemblies are formed at certain concentrations of Sn(II) salt and $Na_2WO_4{\cdot}2H_2O$ in the presence of DNA using microwave heating for 6 min. The average individual size of the particles varies from 1 to 2.5 nm whereas the chain diameter varies from 3 to 11 nm. The potentiality of the $SnWO_4$ nanoassemblies has been tested for the first time in two different applications, such as an anode material in electrochemical supercapacitor studies and as a catalyst for the oxidation of butanol to butanoic acid. From the electrochemical supercapacitor study, it was found that differently sized $SnWO_4$ nanoassemblies showed different specific capacitance (C_s) values and the highest C_s value observed for $SnWO_4$ nanoassemblies having smaller individual particles. The highest C_s value observed was 242 F g^{-1} at a scan rate of 5 mV s^{-1} for small size $SnWO_4$ nanoassemblies. The supercapacitor study

DOI: 10.1021/acssuschemeng.5b00627
ACS Sustainable Chem. Eng. 2015, 3, 2321−2336

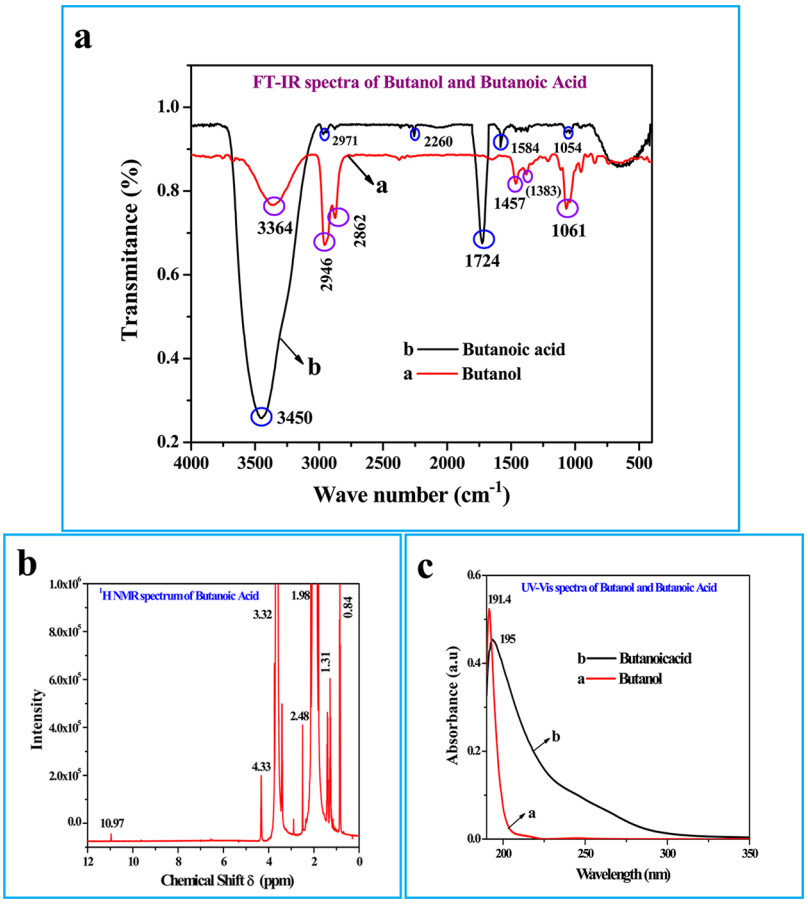

Figure 10. (A) Curve a show the FT-IR spectra of butanol and curve b shows the FT-IR spectra of butanoic acid; (B) ^{1}H NMR spectrum of butanoic acid in the $(CD_3)_2SO_4$ solvent; (C) curve a shows the UV−vis absorption spectra of butanol and curve b shows the absorption spectra of butanoic acid.

showed an excellent long cycle life along with 90% retention of the C_s value even after 1000 consecutive times of cycling at a higher current density of 10 mA cm^{-2}. From the catalysis studies, it was observed that $SnWO_4$ nanoassemblies on a DNA scaffold acted as potential catalysts for the oxidation of butanol to butanoic acid using an eco-friendly hydrogen peroxide as an oxidant with 100% selectivity. Catalysis results signified that both the morphologies showed almost similar catalytic activity due to their ultrasmall size and very low size difference. Other than catalysis and supercapacitor applications, the material can further be used in sensor and visible light photocatalysis applications.

■ ASSOCIATED CONTENT

Supporting Information

The Supporting Information is available free of charge on the ACS Publications website at DOI: 10.1021/acssuschemeng.5b00627.

Details about instrumental characterizations and preparation of samples for various characterizations are elaborated. The figures related to UV−vis transmittance spectra, Field emission scanning electron microscopy (FE-SEM), Energy Dispersive X-ray Spectroscopy (EDS), BET analysis and EIS of $SnWO_4$ before and after 4000 cycles are given in Figure S-1 to S-5 respectively. The data related to FT-IR analysis are provided in Table S-1 (PDF).

■ AUTHOR INFORMATION

Corresponding Author

*S. Kunda. E-mail: skundu@cecri.res.in; kundu.subrata@gmail.com. Phone: (+ 91) 4565-241487. Fax: +91-4565-227651.

Notes

The authors declare no competing financial interest.

■ ACKNOWLEDGMENTS

S. Kundu acknowledges Dr. Vijayamohanan K. Pillai, Director, and Dr. M. Jayachandran, HOD, ECMS division, CSIR-CECRI for their continuous support and encouragement. S. R. Ede acknowledges council of scientific and industrial research (CSIR) for JRF fellowship. The authors thank Mr. S. Anantharaj, ECMS division, CSIR-CECRI for proof reading the entire paper. Authors wish to acknowledge Dr. B. Subramanian, senior scientist, ECMS division, CSIR-CECRI for allowing to use CHI 6034C instrument for electrochemical studies. The institute start-up funding (Project number IHP 0067, DU No. 5, old number OLP-0067), support from the Central Instrumental Facility (CIF), help from Dr. S. Radhakrishnan (NMR in-charge, CIF), Mr. A. Rathishkumar (TEM in-charge, CIF), Mr. J. Kennedy (XPS in-charge, CIF), CSIR-CECRI, Karaikudi are greatly appreciated.

■ REFERENCES

(1) Murphy, C. J. Nanocubes and Nanoboxes. *Science* **2002**, *298*, 2139−2141.

DOI: 10.1021/acssuschemeng.5b00627
ACS Sustainable Chem. Eng. 2015, 3, 2321−2336

(2) Colvin, V. L.; Schlamp, M. C.; Alivisatos, A. P. Light-Emitting Diodes Made from Cadmium Selinide Nanocrystals and a Semiconducting Polymer. *Nature* **1994**, *370*, 354−356.
(3) Hu, J.; Odom, T. W.; Lieber, C. M. Chemistry and Physics in One Dimension: Synthesis and Properties of Nanowires and Nanotubes. *Acc. Chem. Res.* **1999**, *32*, 435−445.
(4) Pech, D.; Brunet, M.; Durou, H.; Huang, P.; Mochalin, V.; Gogotsi, Y.; Taberna, P.-L.; Simon, P. Ultrahigh-power micrometre-sized supercapacitors based on onion-like carbon. *Nat. Nanotechnol.* **2010**, *5*, 651−654.
(5) Conway, B. E. *Electrochemical Supercapacitors-Scientic Fundamentals and Technological Applications*; KluwerAcademic/Plenum Publishers: New York, 1999).
(6) Miller, J. R.; Outlaw, R. A.; Holloway, B. C. Graphene double-layer capacitor with ac line-filtering performance. *Science* **2010**, *329*, 1637−1639.
(7) Rajeswari, J.; Kishore, P. S.; Viswanathan, B.; Varadarajan, T. K. One-dimensional MoO_2nanorods for supercapacitor applications. *Electrochem. Commun.* **2009**, *11*, 572−575.
(8) Nithiyanantham, U.; Ede, S. R.; Anantharaj, S.; Kundu, S. Self-assembled $NiWO_4$ Nanoparticles (NPs) into Chain-like Aggregates on DNA Scaffold with Pronounced Catalytic and Supercapacitor Activities. *Cryst. Growth Des.* **2015**, *15*, 673−686.
(9) Zhang, G. Q.; Lou, X. W. General Solution Growth of Mesoporous $NiCo_2O_4$Nanosheets on Various Conductive Substrates as High-Performance Electrodes for Supercapacitors. *Adv. Mater.* **2013**, *25*, 976−979.
(10) Mai, L. -Q; Yang, F.; Zhao, Y.-L.; Xu, X.; Xu, L.; Luo, Y. − Z. Hierarchical $MnMoO_4/CoMoO_4$ Hetero structured Nanowires with Enhanced Supercapacitor Performance. *Nat. Commun.* **2011**, *2*, 381−385.
(11) Lee, D. G.; Spitzer, U. A. The Aqueous Dichromate Oxidation of Primary Alcohols. *J. Org. Chem.* **1970**, *35*, 3589−3590.
(12) Sato, K.; Aoki, M.; Noyori, R. A. "Green" Route to Adipic acid: Direct Oxidation of Cyclohexenes with 30% Hydrogen Peroxide. *Science* **1998**, *281*, 1646−1647.
(13) Trost, B. M. The Atom Economy a Search for Synthetic Efficiency. *Science* **1991**, *254*, 1471−1477.
(14) Peterson, K. P.; Larock, R. C. Palladium-Catalyzed Oxidation of Primary and Secondary Allylic and Benzylic Alcohols. *J. Org. Chem.* **1998**, *63*, 3185−3189.
(15) Nishimura, T.; Onoue, T.; Ohe, K.; Uemura, S. $Pd(OAc)_2$-catalyzed oxidation of alcohols to aldehydes and ketones by molecular oxygen. *Tetrahedron Lett.* **1998**, *39*, 6011−6014.
(16) Marko, I. E.; Giles, P. R.; Tsukazaki, M.; Brown, S. M.; Urch, C. J. Copper-Catalyzed Oxidation of Alcohols to Aldehydes and Ketones: An Efficient, Aerobic Alternative. *Science* **1996**, *274*, 2044−2046.
(17) Bilgrien, C.; Davis, S.; Drago, R. S. The Selective Oxidation of Primary Alcohols to Aldehydes by Oxygen Employing a Trinuclear Ruthenium Carboxylate Catalyst. *J. Am. Chem. Soc.* **1987**, *109*, 3786−3787.
(18) Scheffer, B.; Molhoek, P.; Moulijn, J. A. Temperature-Programmed Reduction of $NiWO_3/Al_2O_3$ Hydrosulphurization Catalysis. *Appl. Catal.* **1989**, *46*, 11−29.
(19) Wang, H.; Medina, F. D.; Zhou, Y. D.; Zhang, Q. N. Temperature Dependence of the Polarized Raman Spectra of $ZnWO_4$ Single Crystals. *Phys. Rev. B: Condens. Matter Mater. Phys.* **1992**, *45*, 10356−10362.
(20) Yu, S. H.; Liu, B.; Mo, M. S.; Huang, J. H.; Liu, X. M.; Qian, Y. T. General Synthesis of Single-Crystal Tungstate Nanorods/Nanowires: a Facile Low Temperature Solution Approach. *Adv. Funct. Mater.* **2003**, *13*, 639−647.
(21) Jeitschko, W.; Sleight, A. W. Synthesis, Properties and Crystal Structure of β-$SnWO_4$. *Acta Crystallogr., Sect. B: Struct. Crystallogr. Cryst. Chem.* **1972**, *28*, 3174−3178.
(22) Solis, J. L.; Lantto, V. Gas-sensing Properties of Different α-$SnWO_4$-based Thick Films. *Phys. Scr.* **1997**, *T69*, 281−285.
(23) Solis, J. L.; Lantto, V.; Haggstrom, L.; Wikner, M. ^{119}Sn Mössbauer Studies of Stannous Tungstate gas-sensing Semiconductors. *Phys. Rev. B: Condens. Matter Mater. Phys.* **1997**, *2*, 256−260.
(24) Zhang, J.; Liu, Y.; Ke, Y.; Yan, H. Periodic Square-Like Gold Nanoparticle Arrays Templated by Self-Assembled 2D DNA Nanogrids on a Surface. *Nano Lett.* **2006**, *6*, 248−251.
(25) Seeman, N. C. The Design and Engineering of Nucleic acid Nanoscale Assemblies. *Curr. Opin. Struct. Biol.* **1996**, *6*, 519−526.
(26) San Martin, M. C.; Gruss, C.; Carazo, J. M. Six Molecules of SV40 large T antigen Assemble in a Propeller-shaped Particle around a Channel. *J. Mol. Biol.* **1997**, *268*, 15−20.
(27) Solis, J. L.; Frantti, J.; Lantto, V.; Haggstrom, L.; Wikner, M. Characterization of Phase Structures in Semiconducting $SnWO_4$ Powders by Mössbauer and Raman Spectroscopies. *Phys. Rev. B: Condens. Matter Mater. Phys.* **1998**, *57*, 13491.
(28) Dong, H.; Li, Z.; Ding, Z.; Pan, H.; Wang, X.; Fu, X. Nanoplates of α-$SnWO_4$ and SnW_3O_9 prepared via a Facile Hydrothermal Method and their Gas-sensing Property. *Sens. Actuators, B* **2009**, *140*, 623−628.
(29) Cho, I. − S.; Kwak, C. H.; Kim, D. W.; Lee, S.; Hong, K. S. Photophysical, Photoelectrochemical, and Photocatalytic Properties of Novel $SnWO_4$ Oxide Semiconductors with Narrow Band Gaps. *J. Phys. Chem. C* **2009**, *113*, 10647−10653.
(30) Ungelenk, J.; Feldmann, C. Synthesis of faceted β-$SnWO_4$ Microcrystals with Enhanced Visible-light Photocatalytic Properties. *Chem. Commun.* **2012**, *48*, 7838−7840.
(31) Su, Y.; Hou, L.; Du, C.; Peng, L.; Guan, K.; Wang, X. Rapid Synthesis of Zn^{2+} Doped $SnWO_4$ Nanowires with the aim of Exploring Doping Effects on Highly Enhanced Visible Photocatalytic Activities. *RSC Adv.* **2012**, *2*, 6266−6273.
(32) Huang, R.; Ge, H.; Lin, X.; Guo, Y.; Yuan, R.; Fu, X.; Li, Z. Facile one-pot Preparation of α-$SnWO_4$/reduced Graphene oxide (RGO) Nanocomposite with Improved Visible Light Photocatalytic Activity and Anode Performance for Li-ion Batteries. *RSC Adv.* **2013**, *3*, 1235−1242.
(33) Pyper, K. J.; Evans, T. C.; Bartlett, B. M. Synthesis of α-$SnWO_4$ Thin-film Electrodes by Hydrothermal Conversion from Crystalline WO_3. *Chin. Chem. Lett.* **2015**, *26*, 474−478.
(34) Kundu, S.; Peng, L.; Liang, H. A New Route to Obtain High-Yield Multiple Shaped Gold Nanoparticles in Aqueous solution using Microwave Irradiation. *Inorg. Chem.* **2008**, *47*, 6344−6352.
(35) Kundu, S.; Lee, H.; Liang, H. Synthesis and Application of DNA-CdS Nanowires within a Minute using Microwave Irradiation. *Inorg. Chem.* **2009**, *48*, 121−127.
(36) Kundu, S.; Mukadam, M. D.; Yusuf, S. M.; Jayachandran, M. Formation of Shape-selective Magnetic Cobalt Oxide Nanowires: Environmental Application in Catalysis Studies. *CrystEngComm* **2013**, *15*, 482−497.
(37) Kundu, S.; Maheshwari, V.; Niu, S.; Saraf, R. F. Scalable Synthesis of Highly Stable Silver Nanocubes in Less than a Minute under Microwave Irradiation. *Nanotechnology* **2008**, *19*, 65604−65608.
(38) Nithiyanantham, U.; Ede, S. R.; Kesavan, T.; Ragupathy, P.; Mukadam, M. D.; Yusuf, S. M.; Kundu, S. Shape-selective formation of $MnWO_4$ Nanomaterials on DNA Scaffold: Magnetic, Catalytic and Supercapacitor Studies. *RSC Adv.* **2014**, *4*, 38169−38181.
(39) Ede, S. R.; Ramadoss, A.; Nithiyanantham, U.; Anantharaj, S.; Kundu. Bio-molecule Assisted Aggregation of ZnWO4 Nanoparticles (NPs) into Chain-like Assemblies: Material for High Performance Supercapacitor and as Catalyst for Benzyl Alcohol Oxidation. *Inorg. Chem.* **2015**, *54*, 3851−3863.
(40) Kundu, S. A new Route for the Formation of Au Nanowires and Application of Shape-selective Au Nanoparticles in SERS studies. *J. Mater. Chem. C* **2013**, *1*, 831−842.
(41) Nithiyanantham, U.; Ede, S. R.; Kundu, S. Self-assembled Wire-like and Honey-comb like Osmium Nanoclusters (NCs) in DNA with Pronounced Catalytic and SERS Activities. *J. Mater. Chem. C* **2014**, *2*, 3782−3794.
(42) Ede, S. R.; Ramadoss, A.; Anantharaj, S.; Nithiyanantham, U.; Kundu, S. Enhanced Catalytic and Supercapacitor Activities of DNA

DOI: 10.1021/acssuschemeng.5b00627
ACS Sustainable Chem. Eng. 2015, 3, 2321−2336

encapsulated β-MnO_2 Nanomaterials. *Phys. Chem. Chem. Phys.* **2014**, *16*, 21846−21859.
(43) Kundu, S.; Wang, K.; Huitink, D.; Liang, H. Photo-induced Formation of Electrically Conductive Thin Palladium Nanowires on DNA Scaffolds. *Langmuir* **2009**, *25*, 10146−10152.
(44) Kundu, S. Formation of Self-assembled Ag Nanoparticles on DNA chains with Enhanced Catalytic Activity. Phys. *Phys. Chem. Chem. Phys.* **2013**, *15*, 14107−14119.
(45) Jeitschko, W.; Sleight, A. W. Stannous Tungstate: Properties, Crystal Structure and Relationship to Ferroelectric $SbTaO_4$ type Compounds. *Acta Crystallogr., Sect. B: Struct. Crystallogr. Cryst. Chem.* **1974**, *30*, 2088−2094.
(46) Thangavel, S.; Venugopal, G.; Kim, S. − J. Enhanced Photocatalytic Efficacy of Organic Dyes using β-tin Tungstate-reduced Graphene Oxide Nanocomposites. *Mater. Chem. Phys.* **2014**, *145*, 108−115.
(47) Siriwong, P.; Thongtem, T.; Phuruangrat, A.; Thongtem, S. Hydrothermal synthesis, characterization, and optical properties of wolframite $ZnWO_4$ nanorods. *CrystEngComm* **2011**, *13*, 1564−1569.
(48) Ryu, J. H.; Yoon, J. − W.; Lim, C. S.; Oh, W. − C.; Shim, K. B. Microwave Assisted Synthesis of Nanocrystalline MWO_4 (M: Ca, Ni) via Water-based Citrate Complex Precursor. *Ceram. Int.* **2005**, *31*, 883−888.
(49) Caillet, P.; Saumagne, P. Etudes Des Spectres Infrarouges De Polymolymolybdates et Polywolframates Alcalins Anhydres Entre 4000 et 200 cm^{-1}. *J. Mol. Struct.* **1969**, *4*, 351−359.
(50) de Oliveira, A. L. M.; Ferreira, J. M.; Silva, M. R. S.; de Souza, S. C.; Vieira, F. T. G.; Longo, E.; Souza, A. G.; Santos, I. M. G. Influence of Thermal Treatment in the Crystallization of NiWO4 and $ZnWO_4$. *J. Therm. Anal. Calorim.* **2009**, *97*, 167−172.
(51) Mancheva, M. N.; Iordanova, R. S.; Klissurski, D. G.; Tyuliev, G. T.; Kunev, B. N. Direct Mechanochemical Synthesis of Nanocrystaline $NiWO_4$. *J. Phys. Chem. C* **2007**, *111*, 1101−1104.
(52) Banyay, M.; Sarkar, M.; Graslund, A. A Library of IR Bands of Nucleic Acids in Solution. *Biophys. Chem.* **2003**, *104*, 477−488.
(53) Chen, P. C.; Shen, G. Z.; Shi, Y.; Chen, H. T.; Zhou, C. W. Preparation and characterization of flexible asymmetric supercapacitors based on transition-metal-oxide nanowire/single-walled carbon nanotube hybrid thin-film electrodes. *ACS Nano* **2010**, *4*, 4403−4411.
(54) Niu, L.; Li, Z.; Xu, Y.; Sun, J.; Hong, W.; Liu, X.; Wang, J.; Yang, S. Simple Synthesis of Amorphous $NiWO_4$ Nanostructure and Its Application as a Novel Cathode Material for Asymmetric Supercapacitors. *ACS Appl. Mater. Interfaces* **2013**, *5*, 8044−8052.
(55) Simon, P.; Gogotsi, Y. Materials for Electrochemical Capacitors. *Nat. Mater.* **2008**, *7*, 845−854.
(56) Xia, X.; Tu, J.; Zhang, Y.; Wang, X.; Gu, C.; Fan, H. J. High-Quality Metal Oxide Core/ Shell Nanowire Arrays on Conductive Substrates for Electrochemical Energy Storage. *ACS Nano* **2012**, *6*, 5531−5538.
(57) Li, X.; Xiong, S.; Li, J.; Bai, J.; Qian, Y. Mesoporous NiO Ultrathin Nanowire Networks Topotactically Transformed from α-$Ni(OH)_2$ Hierarchical Microspheres and their Superior Electrochemical Capacitance Properties and Excellent Capability for Water Treatment. *J. Mater. Chem.* **2012**, *22*, 14276−14283.
(58) Ramadoss, A.; Kim, S. J. Improved Activity of a Graphene-TiO_2 Hybrid Electrode in an Electrochemical Supercapacitor. *Carbon* **2013**, *63*, 434−445.
(59) Xu, Z.; Li, Z.; Tan, X.; Holt, C.M. B.; Zhang, L.; Amirkhiz, B. S.; Mitlin, D. Supercapacitive Carbon Nanotube-cobalt Molybdate Nanocomposites Prepared *via* Solvent-free Microwave Synthesis. *RSC Adv.* **2012**, *2*, 2753−2755.
(60) Xia, X.; Tu, J.; Zhang, Y.; Wang, X.; Gu, C.; Fan, H. J. High-Quality Metal Oxide Core/ Shell Nanowire Arrays on Conductive Substrates for Electrochemical Energy Storage. *ACS Nano* **2012**, *6*, 5531−5538.
(61) Liu, M. C.; Kong, L. B.; Lu, C.; Li, X. M.; Luo, Y. C.; Kang, L. A Sol-Gel Process for Fabrication of $NiO/NiCo_2O_4/Co_3O_4$ Composite with Improved Electrochemical Behaviour of Electrochemical Capacitors. *ACS Appl. Mater. Interfaces* **2012**, *4*, 4631−4636.
(62) Anantharaj, S.; Nithiyanantham, U.; Ede, S. R.; Kundu, S. Osmium Organosol on DNA: Application in Catalytic Hydrogenation Reaction and in SERS Studies. *Ind. Eng. Chem. Res.* **2014**, *53*, 19228−19238.
(63) Usui, Y.; Sato, K. A Green Method of Adipic Acid Synthesis: Organic Solvent- and Aalide-Free Oxidation of Cycloalkanones with 30% Hydrogen Peroxide. *Green Chem.* **2003**, *5*, 373−375.
(64) Dado, G. P.; Gellman, S. H. Intramolecular Hydrogen Bonding in Derivatives of β-Alanine and γ-Amino Butyric Acid: Model Studies for the Folding of Unnatural Polypeptide Backbones. *J. Am. Chem. Soc.* **1994**, *116*, 1054−1062.
(65) Mallat, T.; Baiker, A. Oxidation of Alcohols with Molecular Oxygen on Solid Catalysts. *Chem. Rev.* **2004**, *104*, 3037−3058.
(66) Shaabani, A.; Mirzaei, P.; Naderi, S.; Lee, D. G.Green Oxidations. The Use of Potassium Permanganate Supported on Manganese dioxide. *Tetrahedron* **2004**, *60*, 11415−11420.
(67) Dijkgraaf, P. J. M.; Duisters, H. A. M.; Kuster, B. F. M.; Vanderwiele, K. Deactivation of platinum catalysts by oxygen: 2. Nature of the catalyst deactivation. *J. Catal.* **1988**, *112*, 337−344.
(68) Vleeming, J. H.; Kuster, B. F. M.; Marin, G. B.Selective Oxidation of Methyl r-D-Glucopyranoside with Oxygen over Supported Platinum: Kinetic Modeling in the Presence of Deactivation by Overoxidation of the Catalyst. *Ind. Eng. Chem. Res.* **1997**, *36*, 3541−3553.

DOI: 10.1021/acssuschemeng.5b00627
ACS Sustainable Chem. Eng. 2015, 3, 2321−2336